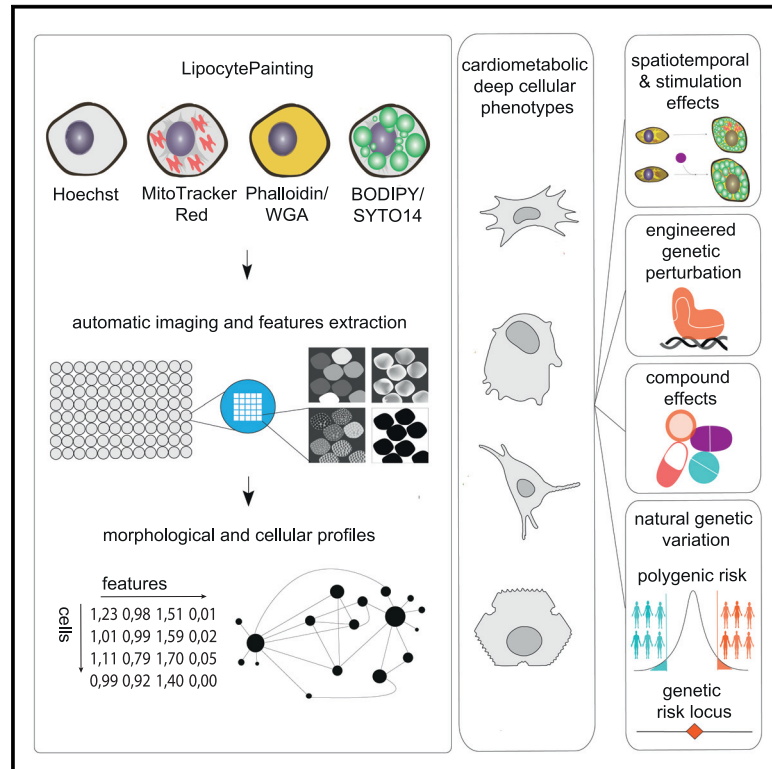# Discovering cellular programs of intrinsic and extrinsic drivers of metabolic traits using LipocyteProfiler

Graphical abstract

Authors

Samantha Laber, Sophie Strobel,
Josep M. Mercader, ..., Cecilia Lindgren,
Suzanne B.R. Jacobs,
Melina Claussnitzer

Correspondence

melina@broadinstitute.org

In brief

Laber and Strobel et al. introduce LipocyteProfiler, a metabolic-disease-oriented image-based deep phenotypic profiling tool, which allows one to systematically link engineered and natural genetic variation as well as chemical perturbations to cell-state-dependent cellular programs in lipocytes. Using LipocyteProfiler, they discover known and novel drivers of cellular programs related to human health and disease.

Highlights

- LipocyteProfiler, a metabolic-disease-oriented image-based phenotypic profiling tool

- LipocyteProfiler links genetic variation, genes, and compounds to cellular programs

- Polygenic metabolic disease risk dictates context-specific cellular programs

- LipocyteProfiler allows us to link variants to function (V2F) without a priori hypotheses

Cell Genomics

Technology

Discovering cellular programs of intrinsic and extrinsic drivers of metabolic traits using LipocyteProfiler

Samantha Laber,[1,2,3,16] Sophie Strobel,[1,5,16] Josep M. Mercader,[1,6,7] Hesam Dashti,[1,7,13] Felipe R.C. dos Santos,[1,13] Phil Kubitz,[1,8,13] Maya Jackson,[1,13] Alina Ainbinder,[1] Julius Honecker,[8] Saaket Agrawal,[1] Garrett Garborcauskas,[1] David R. Stirling,[15] Aaron Leong,[1,6,7] Katherine Figueroa,[1,6] Nasa Sinnott-Armstrong,[1,9] Maria Kost-Alimova,[15] Giacomo Deodato,[1] Alycen Harney,[1] Gregory P. Way,[15] Alham Saadat,[1] Sierra Harken,[1] Saskia Reibe-Pal,[2] Hannah Ebert,[10] Yixin Zhang,[12] Virtu Calabuig-Navarro,[1,10] Elizabeth McGonagle,[1] Adam Stefek,[1] Josée Dupuis,[12,14] Beth A. Cimini,[1] Hans Hauner,[5,8,11] Miriam S. Udler,[1,6,7] Anne E. Carpenter,[15] Jose C. Florez,[1,6,7] Cecilia Lindgren,[1,2,3] Suzanne B.R. Jacobs,[1,6] and Melina Claussnitzer[1,4,6,7,13,17,*]

[1]Programs in Metabolism and Medical and Population Genetics, Type 2 Diabetes Systems Genomics Initiative, Broad Institute of MIT and Harvard, Cambridge, MA 02142, USA
[2]Big Data Institute, Li Ka Shing Centre for Health Information and Discovery, University of Oxford, Oxford OX3 7FZ, UK
[3]Wellcome Centre for Human Genetics, University of Oxford, Oxford OX3 7BN, UK
[4]Massachusetts General Hospital, Harvard Medical School, Boston, MA 02114, USA
[5]Institute of Nutritional Medicine, School of Medicine, Technical University of Munich, 85354 Freising-Weihenstephan, Germany
[6]Diabetes Unit and Center for Genomic Medicine, Massachusetts General Hospital, Boston, MA 02114, USA
[7]Department of Medicine, Harvard Medical School, Boston, MA 02114, USA
[8]Else Kröner-Fresenius-Centre for Nutritional Medicine, School of Life Sciences, Technical University of Munich, 85354 Freising-Weihenstephan, Germany
[9]Department of Genetics, Stanford University, San Francisco, CA, USA
[10]Institute of Nutritional Science, University Hohenheim, 70599 Stuttgart, Germany
[11]German Center for Diabetes Research (DZD), 85764 Neuherberg, Germany
[12]Department of Biostatistics, Boston University School of Public Health, Boston, MA 02118, USA
[13]The Novo Nordisk Foundation Center for Genomic Mechanisms of Disease, Broad Institute of MIT and Harvard, Cambridge, MA 02142, USA
[14]Department of Epidemiology, Biostatistics and Occupational Health, McGill University, Montreal, QC H3A 1G1, Canada
[15]Imaging Platform, Center for the Development of Therapeutics, Broad Institute of MIT and Harvard, Cambridge, MA 02142, USA
[16]These authors contributed equally
[17]Lead contact
*Correspondence: melina@broadinstitute.org
https://doi.org/10.1016/j.xgen.2023.100346

SUMMARY

A primary obstacle in translating genetic associations with disease into therapeutic strategies is elucidating the cellular programs affected by genetic risk variants and effector genes. Here, we introduce LipocyteProfiler, a cardiometabolic-disease-oriented high-content image-based profiling tool that enables evaluation of thousands of morphological and cellular profiles that can be systematically linked to genes and genetic variants relevant to cardiometabolic disease. We show that LipocyteProfiler allows surveillance of diverse cellular programs by generating rich context- and process-specific cellular profiles across hepatocyte and adipocyte cell-state transitions. We use LipocyteProfiler to identify known and novel cellular mechanisms altered by polygenic risk of metabolic disease, including insulin resistance, fat distribution, and the polygenic contribution to lipodystrophy. LipocyteProfiler paves the way for large-scale forward and reverse deep phenotypic profiling in lipocytes and provides a framework for the unbiased identification of causal relationships between genetic variants and cellular programs relevant to human disease.

INTRODUCTION

With the rise of human genome sequencing data, the number of genetic variants known to be associated with human diseases has increased substantially; however, elucidating the pathogenic mechanisms through which genetic variants impact disease remains limiting. Phenotypic profiling is a powerful tool to systematically discover external and internal regulators of biological processes in cellular systems in an unbiased manner.[1–4] High-content imaging is an established multi-parametric approach that captures and quantifies biological processes from microscopy images, yielding a rich set of morphological and cellular profiles.[5] To date, image-based profiling has been used in small-molecule screens to identify compound
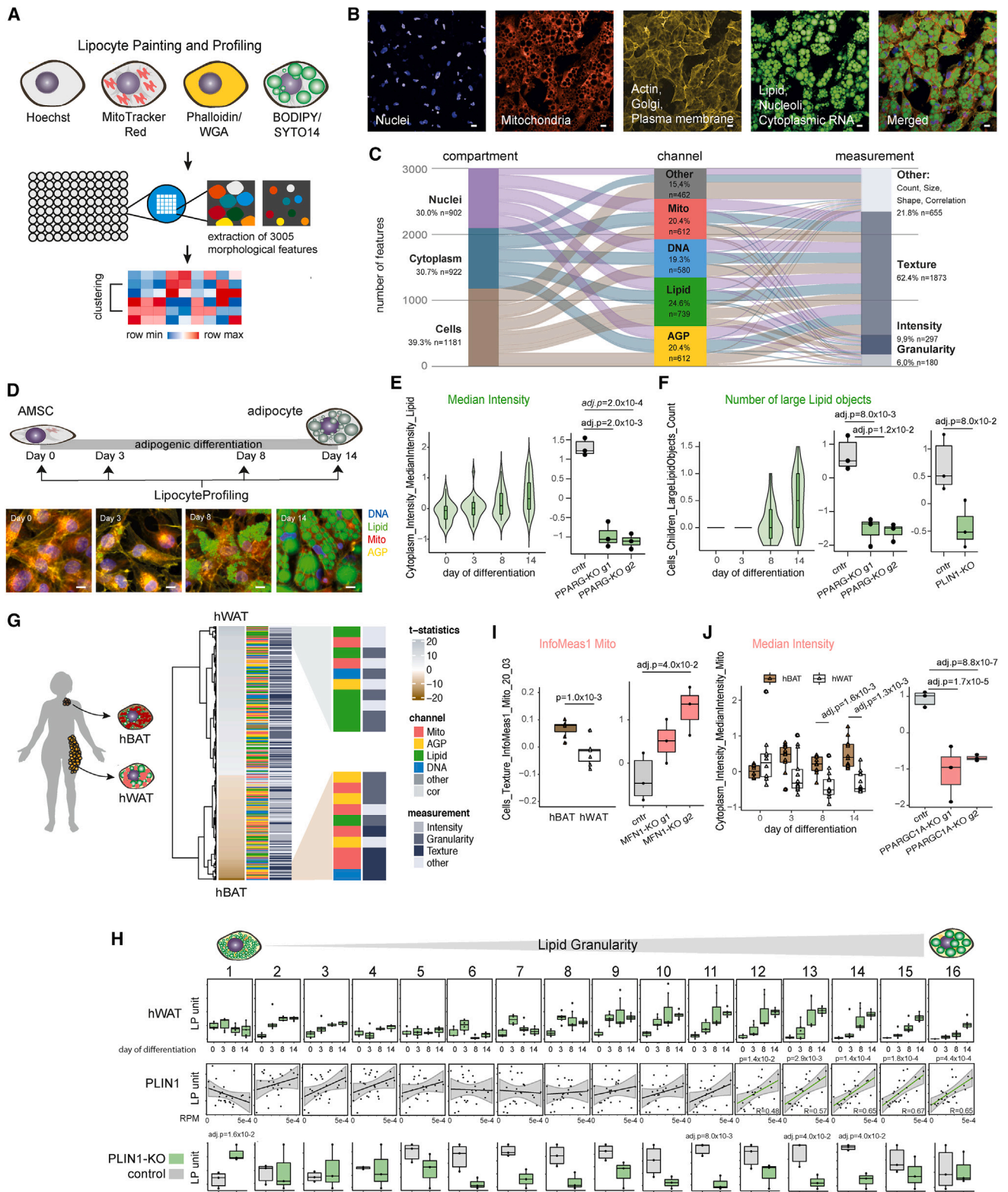
Figure 1. LipocyteProfiler creates rich morphological and cellular profiles in adipocytes that are informative for known cellular functions

(A) Schematic of LipocyteProfiler, which is a high-content imaging assay that multiplexes six fluorescent stains imaged in four channels in conjunction with an automated image-analysis pipeline to generate rich morphological and cellular profiles in lipid-storing cell types (lipocytes), such as adipocytes during differentiation.

(legend continued on next page)

fingerprints, ascertain compound toxicity, and predict compound assay activity[6–9] and in gene expression screens to annotate gene function.[10] In all cases, the basic strategy is to match the profile of a given sample based on similarity to morphological profiles of previously annotated samples.

In metabolism, lipid droplets represent a relevant feature that is amenable to image-based profiling. Lipid droplets are storage organelles central to both whole-body metabolism and energy homeostasis. These droplets are highly dynamic and found in all cell types.[11] They are functional in either cellular homeostasis in lipid-accumulating cells (lipocytes), such as adipocytes, hepatocytes, macrophages/foam cells, and glial cells,[11–15] or in pathophysiological processes in cells including vascular smooth muscle cells, skeletal muscle cells, renal podocytes, and cancer cells.[16–20] Changes in lipid-droplet dynamics such as the number and size of lipid droplets and overall lipid content are associated with the progression of numerous metabolic diseases including type 2 diabetes (T2D), obesity, and non-alcoholic fatty liver disease.[21]

Here, we introduce LipocyteProfiler, a metabolic-disease-oriented phenotypic profiling system for lipid-accumulating cells bridging the gap between high-throughput generalizable assays and low-throughput, highly customized, disease-focused readouts. LipocyteProfiler is an adaptation of Cell Painting[5,22–24] that incorporates BODIPY to measure dynamic features of lipid droplets and thus captures lipocyte-relevant phenotypes in addition to generic morphological profiles.

Design

Elucidating cellular programs that underlie the association of genetic variants, regulatory elements, and genes with diseases largely remains a non-systematic, labor- and cost-intensive endeavor that is biased toward hypotheses drawn from a priori knowledge. High-content imaging captures and quantifies numerous distinct biological processes from microscopy images in an unbiased manner, yielding a rich set of morphological and cellular profiles.[5]

Thus far the phenotypic data ascertained from scalable morphological profiling assays has been limited to features informative for the generic organelles of the cell.[5,22,23] This includes structural information about nuclei, endoplasmic reticulum, cytoskeleton, and mitochondria, or generic processes, such as cell growth or proliferation. It is currently unknown how gene and compound effects translate to changes in specific cellular pathways and processes. Image-based deep cellular phenotypic profiling tools provide a plethora of quantitative features. However, narrowing down these high-dimensional data matrices to a set of the most informative features that drive cellular processes requires differentiating first-order from second-order relationships among the features. As such, there is a pressing need to develop foundational technologies that allow systematic linking of genetic variation to disease-relevant cellular programs at scale and in a broadly accessible way.

To quantitatively map dynamic and context-dependent morphological and cellular signatures in lipocytes as well as discover intrinsic and extrinsic drivers of cellular programs, we developed a high-content image-based profiling approach called LipocyteProfiler (Figure 1A). LipocyteProfiler is an unbiased high-throughput profiling assay that generates rich generic and lipocyte-specific cellular profiles from six multiplexed fluorescent dyes imaged in four channels (Figure 1B) in conjunction with an automated image-analysis pipeline (see STAR Methods and Method S1).

LipocyteProfiler extracts 3,005 morphological and cellular features that map to three cellular compartments (Cell, Cytoplasm, and Nucleus) across four organelles, namely nucleus (Hoechst), *Mito* (MitoTracker red, which stains mitochondria), *AGP* (actin, Golgi, plasma membrane; stained with phalloidin [F-actin cytoskeleton] and wheat germ agglutinin [Golgi and plasma membranes]), and *Lipid* (BODIPY, which stains neutral lipids,

(B) Representative microscopy image of fully differentiated adipocytes for four individual channels and a merged representation across channels. Scale bars, 10 μm.

(C) LipocyteProfiler extracts 3,005 morphological and cellular features that map to three cellular compartments and across four channels using four measurement classes.

(D) Schematic of LipocyteProfiling in differentiating hWAT at four time points of adipocyte differentiation (days 0, 3, 8, 14). Representative images of AMSCs stained using LipocytePainting at four time points of differentiation (days 0, 3, 8, 14). Scale bars, 10 μm.

(E) Cytoplasm *MedianIntensity Lipid*, a measurement of lipid content within a cell, significantly increases with adipogenic differentiation and decreases following CRISPR-Cas9-mediated knockdown of *PPARG* in differentiated white adipocytes. Data are shown for two guides used (g1 and g2), and y axis shows LP units (normalized LipocyteProfiling [LP] values across three batches, see STAR Methods).

(F) *Number of large Lipid objects* informative for large lipid droplets are absent in the progenitor state (day 0) and in early differentiation (day 3) and progressively increase in later stages of differentiation (days 8 and 14). *Number of large Lipid objects* is reduced following CRISPR-Cas9-mediated knockout (KO) of *PPARG* (data are shown for two guides used [g1 and g2]) and *PLIN1*, at day 14 of differentiation. y axis shows LP units (normalized LP values across three batches, see STAR Methods).

(G) Morphological profiles of white (hWAT) and brown (hBAT) adipocytes at day 14 of differentiation differ significantly across all feature classes (FDR < 0.1%). Features are clustered based on effect size. Features with the highest effect size in hWAT and hBAT adipocytes are lipid- and mitochondria-related, respectively. Graph shows zoom-in for top ten features with largest effect sizes in hWAT (top panel) and hBAT (bottom panel).

(H) *Lipid* Granularity measures, as spectra of 16 lipid-droplet size measures, show size-specific changes in hWAT and hBAT during differentiation. See also Figure S1H. Granularity features informative for larger lipid droplets (*Lipid Granularity* 10–16) correlate positively with *PLIN1* gene expression and are reduced in *PLIN1*-KO adipocytes. See also Figures S1I and S1J (PLIN2, FASN-KO). y axis shows autoscaled LP units (normalized LP values across three batches, seeSTAR Methods).

(I) Brown adipocytes (hBAT) show higher *Mito_Texture_InfoMeas1*, a measure of spatial relationship between specific intensity values, compared with white adipocytes (hWAT). CRISPR-Cas9-mediated knockout of *MFN1*, a mitochondrial fusion gene, changes *Mito_Texture_InfoMeas1* (data shown for two guides used [g1 and g2]). y axis shows LP units (normalized LP values across three batches [hBAT/hWAT] or normalized across CRISPR-KO data, see STAR Methods).

(J) *Mito_MedianIntensity* is higher in brown (hBAT) compared with white (hWAT) adipocytes throughout differentiation and decreased after CRISPR-Cas9-mediated knockout of *PPARGC1A* in hWAT. y axis shows LP units (normalized LP values across three batches, see STAR Methods).

multiplexed with SYTO14, which stains nucleoli and cytoplasmic RNA) (Figures 1C and S1A). Within each compartment and channel, features quantify morphological changes based on four different measurement classes: *Intensity*, *Granularity*, *Texture*, and *Others* (Figures 1C and S1A).

More specifically, *Intensity* features are a collection of features that measure pixel intensities across an image using various measurement types such as *MedianIntensity*, *MaxIntensity*, and *RadialDistribution* of Intensity. Texture features describe the complexity or homogeneity within an image of a compartment using a plethora of different quantification approaches including *Entropy*, *AngularSecondMoment*, and *Variance* measurements. *Granularity* features are informative for a spectrum of different structural elements (sizes 1–16) that fit into an image. For example, *Granularity Lipid* features are indicative for small (sizes 1–5), medium (sizes 6–10), and large (sizes 11–16) lipid droplets. The fourth measurement class, referred to as *Other* features, is a composition of different measurements that quantify *shape*, *size*, and *count* of cells as well as correlations between different channel intensities (e.g., between *Mito* and *Lipid*). In concert, these features build rich lipocyte-specific cellular profiles that enable elucidation of cellular programs that link genetic loci and variation to human disease.

To nominate LipocyteProfiler core features that drive cellular processes we applied an information theoretic algorithm, which reduces the 3,005 LipocyteProfiler features, based on mutual information (MI) between features, and prioritizes first-order interactions indicative of direct interactions between features[25–27] (Figure S1B). By representing features as nodes of a graph and MI-based calculated interactions between features as weighted edges, we constructed an MI network representing interactions between the features. After ranking the nodes based on their degree of connectivity (number of edges), we defined LipocyteProfiler core features as those features among the 75% upper quantile of the ranked nodes and the lower 25% percentile of the average MI. The MI-based feature reductions allowed us to nominate approximately one-third of the features as core features (Figures S1B and S1C) that can be used to identify intrinsic and extrinsic drivers of phenotypic changes in a concise way.

We demonstrate that our LipocyteProfiler tool can identify diverse cardiometabolic-disease-relevant cellular mechanisms by generating context-, process-, and allele-specific morphological and cellular profiles. We prototyped LipocyteProfiler in adipocytes and hepatocytes, which are highly specialized cells that store excess energy in the form of lipid droplets and have key roles in cardiometabolic disease. First, we demonstrate that LipocyteProfiler can identify meaningful changes in feature profiles (1) during adipocyte differentiation, (2) across white and brown adipocyte lineages, and (3) following genetic and drug perturbations. Next, we correlated LipocyteProfiler features with transcriptomic data from RNA sequencing (RNA-seq) to link gene sets with morphological and cellular features, capturing a broad range of cellular activity in differentiating adipocytes. We then applied LipocyteProfiler to connect polygenic risk scores for type 2 diabetes (T2D)-related traits to cellular phenotypes and discover novel trait-specific cellular mechanisms underlying polygenic risk. Finally, we used our method to uncover cellular traits under the genetic control of

an individual genetic risk locus, demonstrated for the *2p23.3* metabolic risk locus at *DNMT3A*.[28]

RESULTS

LipocyteProfiler generates meaningful morphological and cellular profiles in differentiating adipocytes

To test the ability of LipocyteProfiler to extract biologically meaningful high-dimensional representations of morphological and cellular programs, we used our metabolic-disease-oriented image-based profiling tool to detect (1) changes associated with adipocyte differentiation, (2) differences between white and brown adipocytes, and (3) phenotypic effects of directed gene perturbation using CRISPR-Cas9 to knock out key regulators of adipocyte function.

First, we applied LipocyteProfiler to a model of adipocyte differentiation using an established white adipocyte line (hWAT),[29] which undergoes phenotypic changes from fibroblast-shaped to spherical lipid-filled cells during differentiation (days 0, 3, 8, and 14; Figure 1D). We mapped the phenotypic signature of progressive lipid accumulation and cytoskeletal remodeling during adipocyte differentiation in hWAT using tractable *Lipid* and *AGP* features. We show that cytoplasmic intensity of *Lipid*, a proxy of overall lipid content within a cell, increased with adipogenic differentiation (Figure 1E). In addition, *large Lipid objects* (large lipid droplets) were absent in the progenitor state (day 0) and in early differentiation (day 3), and the number of these objects increased in later stages of differentiation (Figure 1F). We confirmed that CRISPR-Cas9-directed perturbation of *PPARG*, the master regulator of adipogenesis, decreases the overall *Lipid Intensity* in differentiated white adipocytes (guide 1 adjusted p [adj.p] = 2.0×10^{-3}, guide 2 adj.p = 2.0×10^{-4}; Figure 1E). Furthermore, *large Lipid objects* present at day 14 of differentiation were reduced when we perturbed regulators of lipid accumulation, *PPARG* (guide 1 adj.p = 8.0×10^{-3}, guide 2 adj.p = 1×10^{-2}) and *PLIN1* (adj.p = 8.0×10^{-2}), a key regulator of lipid-droplet homeostasis (Figure 1F). These data demonstrate that LipocyteProfiler detects expected changes in lipid dynamics associated with adipocyte differentiation. Another cellular change that occurs during adipocyte differentiation is a drastic reorganization of the actin cytoskeleton, which transitions from well-defined stress fibers in pre-adipocytes to relatively thick cortical actin lining composed of patches of punctate F-actin at the inner surface of the plasma membrane in fully differentiated adipocytes[30] (Figure S1D). This cytoskeletal remodeling is stimulated by insulin and essential for GLUT4 translocation into the membrane to facilitate insulin-responsive glucose uptake in the cell.[30] Concordantly, we found that CRISPR-Cas9-mediated disruption of the insulin receptor (*INSR*) and insulin receptor substrate 1 (*IRS1*) in pre-adipocytes altered *AGP Texture* features (describing the smoothness of a given stain) in mature adipocytes at day 14 of differentiation (Figure S1E). Specifically, *INSR* and *IRS* knockout reduced variation of cytoplasmic *AGP* stain intensities most significantly near the plasma membrane (Cytoplasm_RadialDisribution_RadialCV_AGP_4_of_4, *IRS1* guide 1 adj.p = 8.0×10^{-3}, guide 2 adj.p = 8.0×10^{-2}; *INSR* guide 1 adj.p = 8.0×10^{-2}, guide 2 adj.p = 2.0×10^{-2}), indicative of less punctuated *AGP*, which is in line with less cortical actin in *INSR*- and *IRS*-knockout cells.
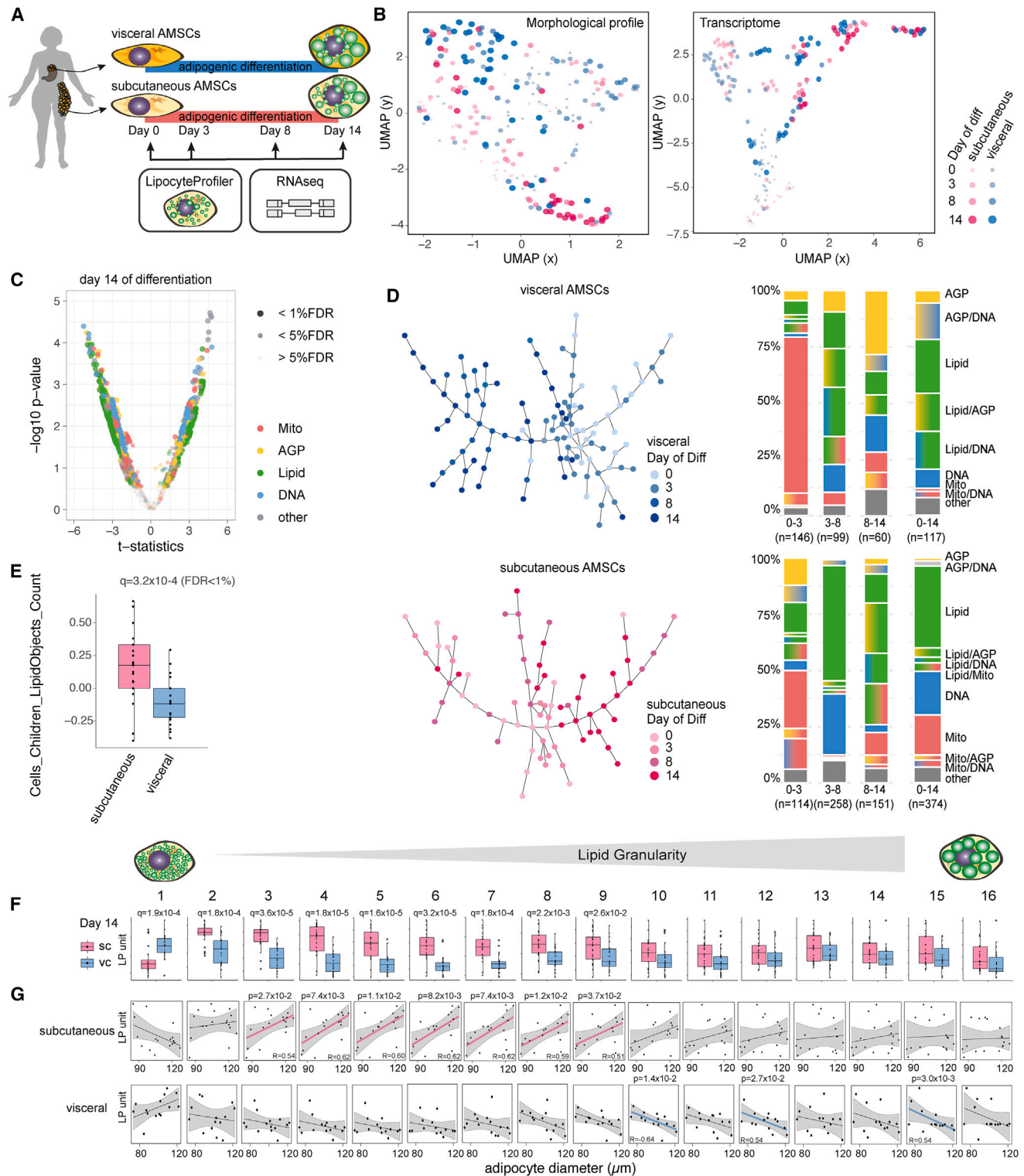
Figure 2. LipocyteProfiler identifies distinct depot-specific morphological and cellular signatures associated with differentiation trajectories in both visceral and subcutaneous AMSCs

(A) Human AMSCs isolated from subcutaneous and visceral adipose depots were differentiated for 14 days, and LipocyteProfiler and RNA-seq profiling were performed throughout adipocyte differentiation (days 0, 3, 8, and 14).

Next, we used brown and white adipocyte model systems to elucidate mitochondrial and lipid-related informational content. Intrinsic differences distinguishing white and brown adipocytes are known to be predominantly driven by differences in mitochondrial number and activity that translate into differential lipid accumulation.[31] Using an established brown adipocyte line derived from human neck fat (hBAT) from the same individual as for the hWAT line, we showed that morphological profiles from differentiated hWAT and hBAT differ significantly in every channel and feature category (Figure 1G). *Lipid Granularity* measures, a class of metrics that capture the typical sizes of bright spots for a stain, predominated among those increased in hWAT. During adipocyte differentiation, lipid droplets typically increase first in number and then enlarge and fuse to form larger lipid droplets over the course of maturation.[32] We observed that the number of small and medium-sized lipid droplets (*Lipid Granularity* measures 1–9) present in early differentiating hWAT saturate in early stages of differentiation (Figure 1H). Larger lipid droplets (*Lipid Granularity* measures 10–16) increase in terminal differentiation, indicating that lipid droplets form in early differentiation and grow thereafter, a process that is reflected in *Lipid Granularity* measures and *Lipid objects* count (Figures 1H and S1F). Consistent with the notion that adipocytes from brown adipose have smaller lipid droplets, we found that during differentiation, hBAT adipocytes accumulate fewer medium-sized and large lipid droplets as seen by lower values across the spectra of granularity (Figures 1H and S1G). Intuitively, LipocyteProfiler-derived size estimates showed that white hWAT are larger than brown hBAT adipocytes after 14 days of adipogenic differentiation as cells become lipid laden (*Cells_AreaShape_Area* p = 5.1×10^{-5}; Figure S1H). To test whether lipid-droplet-associated perilipins can be linked to lipid-droplet sizes, we correlated *Lipid Granularity* measures with mRNA expression levels of *PLIN1*, which is specifically expressed in adipocytes where it directs the formation of large lipid droplets[33,34] and *PLIN2*, the only constitutively and ubiquitously expressed lipid-droplet protein that is associated with a range of lipid droplets in diverse cell types.[35,36] We observed that mRNA expression levels of *PLIN1* positively correlated with the *Lipid Granularity* features informative for larger spot sizes (*Lipid Granularity* measures 12–16) (Figure 1H). *PLIN2* correlated best with *Lipid Granularity* measures of smaller and larger spectra (Figure S1I). Accordingly, when we knocked out *PLIN1* and *FASN*, genes involved in lipid-droplet dynamics and lipid metabolism, we observed a size-specific reduc-

tion of *Lipid Granularity* (Figures 1H and S1J), suggesting that *Lipid Granularity* features are a suitable output measure of lipid-droplet size spectra and an indicator of adipocyte differentiation.

Consistent with the relevance of mitochondria for brown adipocyte function, mitochondrial measures were among the features that increased the most in hBAT (Figure 1G), particularly the *Texture* feature *Cells_Texture_InfoMeas1_Mito* (p = 1.0×10^{-3}), which describes the overall information content based on the smoothness of a given stain. Perturbation of *MFN1*, a mitochondrial fusion gene, increased *Cells_Texture_InfoMeas1_Mito* in hWAT adipocytes (adj.p = 4.0×10^{-2}; Figure 1I), suggesting that the higher values of this measurement in differentiated hBAT could be indicative of higher mitochondrial fission in hBAT compared with hWAT. This finding is consistent with brown adipocytes elevating mitochondrial thermogenesis by increasing mitochondrial fission.[37] hBAT adipocytes are further characterized by increased *Mito Intensity* compared with hWAT adipocytes throughout differentiation, with the most substantial increase in the fully differentiated state (median, day 8 adj.p = 1.6×10^{-3}, day 14 adj.p = 1.3×10^{-3}; Figure 1J), demonstrating that LipocyteProfiler can identify known cellular programs that distinguish different adipocyte lineages. Indeed, when we perturbed *PPARGC1A*, the master regulator of mitochondrial biogenesis and thermogenesis in adipocytes, using CRISPR-Cas9-mediated knockout in hWAT, mitochondrial intensity decreased (guide 1 adj.p = 1.7×10^{-5}, guide 2 adj.p = 8.8×10^{-7}; Figure 1J). We also confirmed similar morphological and cellular differences between brown hBAT adipocytes and another established white adipocyte cell line, differentiated SGBS (Simpson-Golabi-Behmel syndrome) cells (Figure S2A). Taken together, our data demonstrate that LipocyteProfiler can generate rich sets of morphological and cellular features that correlate with cellular function.

LipocyteProfiler identifies distinct depot-specific signatures associated with differentiation trajectories in visceral and subcutaneous adipocytes

We next used LipocyteProfiler to distinguish phenotypes of primary human adipose-derived mesenchymal stem cells (AMSCs) derived from the two main adipose tissue depots in the body, namely subcutaneous and visceral, across the course of differentiation (Figure 2A). We differentiated subcutaneous and visceral AMSCs and generated morphological profiles at days 0, 3, 8, and 14 using LipocyteProfiler and validated

(B) LipocyteProfiler and transcriptome profiles show time-course-specific signatures revealing a differentiation trajectory, but only LipocyteProfiler additionally resolves adipose-depot-specific signatures.

(C) Subcutaneous and visceral AMSCs at terminal differentiation (day 14) have distinct morphological and cellular profiles with differences that are spread across all channels. See also Figure S2C (volcano plot reporting the $-\log_{10}$ p value and the effect comparing subcutaneous and visceral adipocytes, t test).

(D) Sample progression discovery analysis (SPD). Proportions of subgroups of features characterizing differentiation differ between subcutaneous and visceral adipocytes and dynamically change over the course of differentiation. In both depots, *Mito* features drive differentiation predominantly in the early phase of differentiation (days 0–3) whereas *Lipid* features predominate in the terminal phases (days 8–14). See also Figure S2D for SPD of hWAT and SGBS.

(E) The number of lipid droplets is higher in subcutaneous AMSCs than in visceral AMSCs at terminal differentiation. y axis shows LP units (normalized LP values across eight batches, see STAR Methods).

(F) Mature subcutaneous AMSCs have larger intracellular lipid droplets compared with visceral AMSCs at day 14 of differentiation (*Lipid Granularity*). y axis shows autoscaled LP units (normalized LP values across eight batches, see STAR Methods).

(G) *Lipid Granularity* from subcutaneous AMSCs at day 14 of differentiation correlates positively with floating mature adipocyte diameter but shows an inverse relationship for visceral adipose tissue, suggesting distinct cellular mechanisms that lead to adipose tissue hypertrophy in these two depots. y axis shows autoscaled LP units (normalized LP values across eight batches; x axis, histology adipocytes diameter [μm], see STAR Methods).

successful differentiation in both depots by an increase of adipogenesis marker genes (*LIPE*, *PPARG*, *PLIN1*, *GLUT4*) (Figure S2B). Concomitantly, we used RNA-seq to profile the transcriptome on the same differentiation time points. We observed that both the morphological and transcriptomic profiles show time-course-specific signatures revealing a differentiation trajectory; however, only morphological profiles generated by LipocyteProfiler also resolved adipose-depot-specific signatures throughout differentiation (Figure 2B). At day 14 of differentiation, morphological differences between subcutaneous and visceral adipocytes were spread across a large number of features in all feature classes (Figures 2C and S2C).

To discover patterns associated with progression through adipocyte differentiation in each depot, we performed a sample progression discovery analysis (SPD).[38] SPD clusters samples to reveal their underlying progression and simultaneously identifies subsets of features that show the same progression pattern and are illustrative of differentiation. We discovered that subsets of features distinguish the differentiation patterns of subcutaneous and visceral adipocytes and that most dominant feature classes were dynamically changing over the time course of differentiation (Figure 2D). In visceral adipocytes, the early phase of differentiation was predominantly associated with mitochondrial features, whereas terminal phases of differentiation were primarily associated with changes in lipid-related features (Figure 2D). In subcutaneous adipocytes, we observed that the feature classes (actin cytoskeleton, lipid, mitochondrial, and nucleic acid) were more evenly involved through adipogenesis and that the contribution of *Lipid* features started in early phases of differentiation, consistent with an earlier initiation of lipid accumulation in subcutaneous compared with visceral adipocytes (Figure 2D). To demonstrate that LipocyteProfiler captures consistent morphological patterns across white adipocyte models, we applied SPD to differentiate white adipocytes and show that SGBS cells, the immortalized subcutaneous hWAT line, and subcutaneous AMSCs progress similarly throughout adipocyte differentiation (Figure S2D). More specifically, we show that among the feature classes, *Lipid* features contribute the most to dynamical changes during adipocyte differentiation. SGBS cells begin the differentiation process by initiating the formation of lipid droplets (percentage of *Lipid* features between day 0 and day 3), which grow in the later stages (contribution of *AGP* features between days 8 and 14). These dynamic changes are similar to morphological changes of subcutaneous adipocytes and indicate that LipocyteProfiler can capture cell-specific morphological characteristics.

We next compared lipid-related signatures in mature AMSCs and observed that subcutaneous AMSCs had more lipid droplets than visceral AMSCs (*Cells_LipidObject_count*, Figure 2E, q = 3.2×10^{-4}, false discovery rate [FDR] < 1%). More specifically, mature subcutaneous AMSCs showed significantly higher *Lipid Granularity* of small to medium-sized lipid objects, whereas visceral adipocytes showed higher *Lipid Granularity* of very small lipid objects, suggesting that mature subcutaneous AMSCs have larger intracellular lipid droplets compared with visceral AMSCs, which present higher abundance of very small lipid droplets (Figure 2F). These apparent intrinsic differences in differentiation capacity and lipid accumulation between subcu-

taneous and visceral AMSCs are consistent with previously described distinctions between AMSC depot properties across differentiation.[39] Our data suggest that LipocyteProfiler can facilitate identification of distinct lineage differences and programs of cellular differentiation.

Lastly, to assess the *in vivo* relevance of morphological features of *in vitro* differentiated adipocytes, we correlated *Lipid Granularity* features of adipocytes at day 14 of differentiation with diameter estimates of tissue-derived mature adipocytes from the same individual (see STAR Methods). We showed that changes in *Lipid Granularity* of *in vitro* differentiated female subcutaneous adipocytes correlated significantly with the mean diameter of mature adipocytes (Figure 2G). More specifically, medium-size granularity measures increased with larger *in vivo* size estimates, suggesting that *in vivo* adipocyte size is reflected by medium-sized lipid droplets in subcutaneous adipocytes that have been differentiated *in vitro*. Strikingly, we found the opposite effect between correlation of visceral *Lipid Granularity* and diameter estimates from mature adipocytes, suggesting that subcutaneous and visceral adipose tissues differ in cellular programs that govern depot-specific adipose tissue expansion, which may account for different depot-specific susceptibility to metabolic diseases. Indeed, white adipose depots have been reported to differ in their respective mechanisms of fat mass expansion under metabolic challenges, with subcutaneous adipose tissue being more capable of hyperplasia whereas visceral adipose tissue expands mainly via hypertrophy.[40]

LipocyteProfiler features reflect transcriptional states in adipocytes

To identify relevant processes that manifest in morphological and cellular features and to identify pathways of a given set of features, we next used a linear mixed model to link the expression of 52,170 genes derived from RNA-seq with each of the image-based LipocyteProfiler features in subcutaneous adipocytes at day 14 of differentiation across 26 individuals (Figure 3A and STAR Methods). We found 20,296 non-redundant significant feature-gene connections that were composed of 7,012 genes and 669 features (FDR < 0.01%, Figure 3B and Table S1A; FDR < 0.1%: 44,736 non-redundant feature-gene connections, 10,931 genes and 869 features, Figure S3A and Table S1B), and mapped across all channels (Figure 3A). Although features from every channel had significant gene correlations, *Lipid* features showed the highest number of gene connections compared with any other channel. This suggests that lipid-droplet structure, localization, and dynamics in adipocytes most closely represent the transcriptional state of the differentiated cell (Figure 3B). Pathway enrichment analyses of lists of genes connected to a feature at FDR < 0.01% add support to the idea that genes that correlated with a particular feature are biologically meaningful. For example, *Mito Granularity* associated with genes that are enriched for pathways such as the tricarboxylic acid cycle (TCA), which oxidizes acetyl-coenzyme A in mitochondria,[41] and lipid and lipoprotein metabolism and triglyceride biosynthesis, which are known to involve mitochondrial processes (pathway enrichment analysis FDR < 5%). This connection between lipid and mitochondrial processes was also detected in feature-gene associations for *Lipid Intensity*,
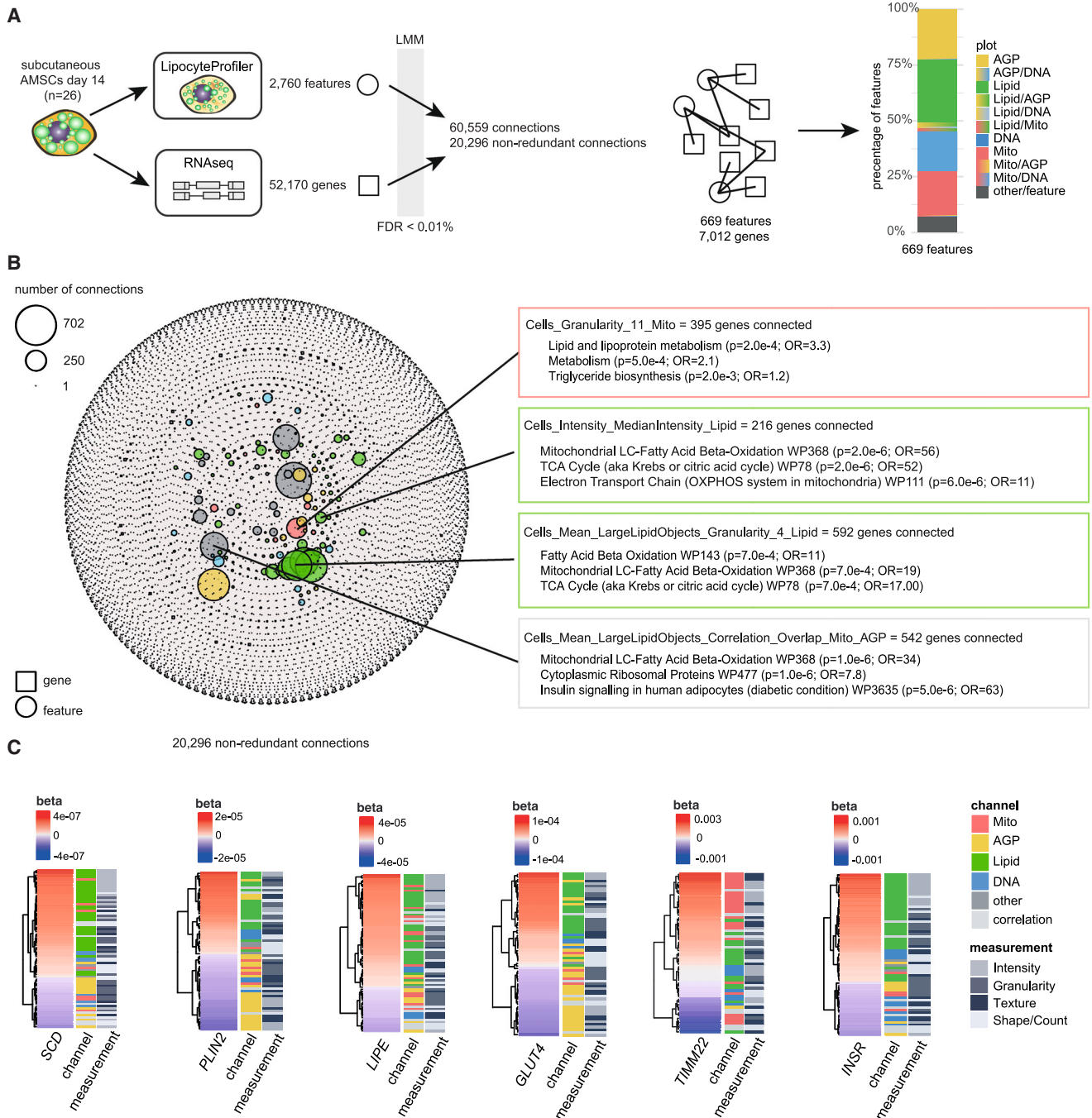
Figure 3. Correlations between morphological and transcriptional profiles

(A) Linear mixed model (LMM) was applied to correlate 2,760 morphological features derived from LipocyteProfiler with 52,170 transcripts derived from RNA-seq in matched samples of subcutaneous AMSCs at terminal differentiation (day 14). With FDR < 0.01%, we discover 20,296 non-redundant connections that map to 669 morphological features and 7,012 genes.

(B) Network of transcript-LipocyteProfiler feature correlations (significant connections FDR < 0.01%). Genes correlated with individual LipocyteProfiler features are enriched for relevant pathways (FDR < 5%). Node size is determined by number of connections. See also Figure S3A for a network with a significance level threshold of FDR < 0.1%.

(C) LipocyteProfiler signatures of adipocyte marker genes *SCD*, *PLIN2*, *LIPE*, *GLUT4*, *TIMM22*, and *INSR* recapitulate their known cellular function. Features are clustered based on beta of linear regression.
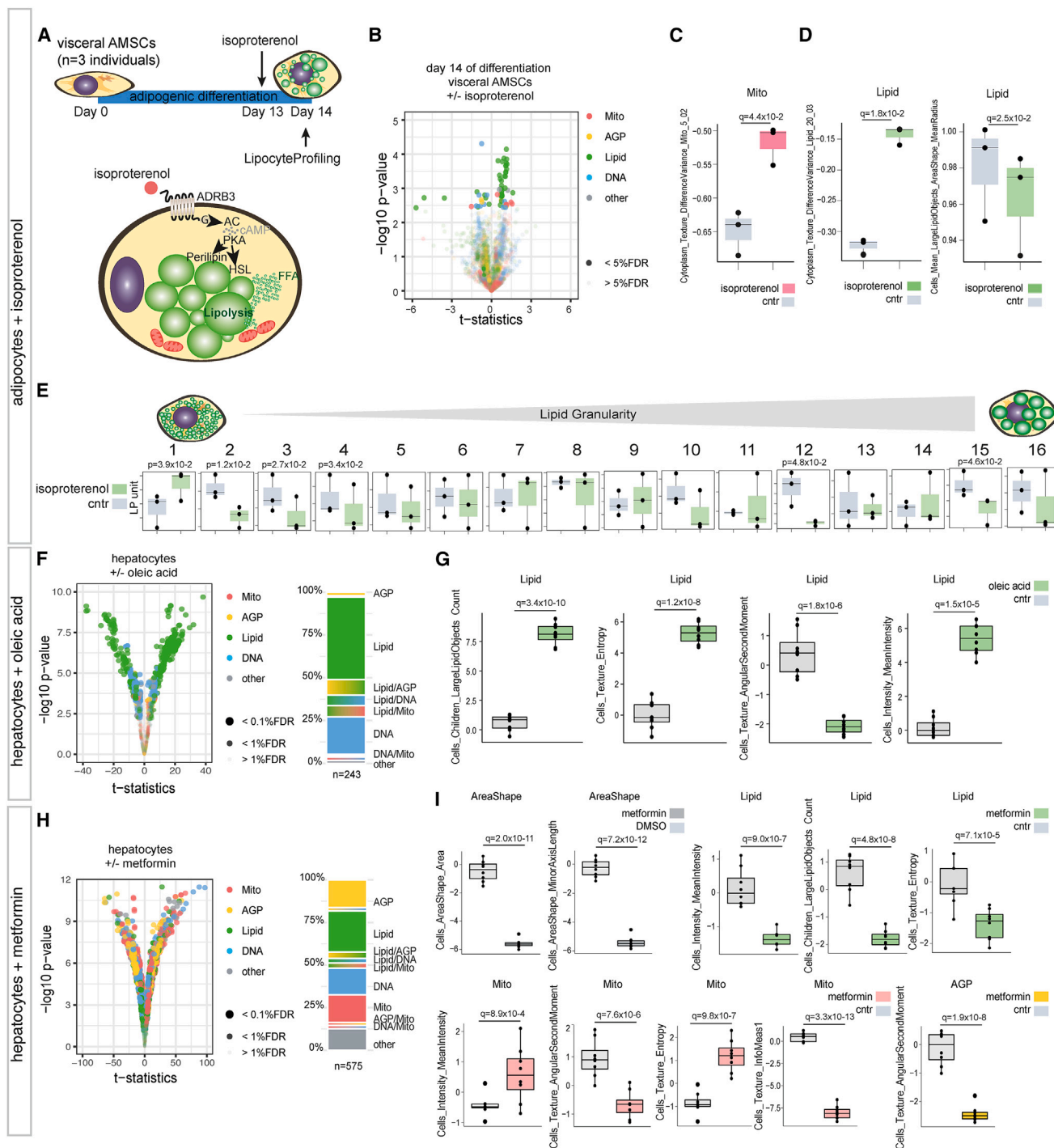
Figure 4. LipocyteProfiler identifies molecular mechanisms of drug stimulations in adipocytes and hepatocytes

(A) LipocyteProfiler was performed in visceral AMSCs (n = 3) treated with the β-adrenergic receptor agonist isoproterenol for 24 h.

(B) Isoproterenol treatment results in changes of lipid-related and mitochondrial traits in visceral AMSCs at day 14 of differentiation. See also Figure S3B (volcano plot reporting the $-\log_{10}$ p value and the effect comparing isoproterenol-treated cells and DMSO-treated cells, t test).

(C and D) Isoproterenol treatment of visceral AMSCs increase *Mito* and *Lipid TextureDifferenceVariance* while decreasing the respective *LargeLipidObject* mean radius features. y axis shows LP units (normalized LP values across eight batches, see STAR Methods).

(E) Isoproterenol treatment reduces lipid-droplet sizes measured via lipid granularity. y axis shows autoscaled LP units (normalized LP values across eight batches, see STAR Methods).

(F) Oleic acid treatment in PHH results in changes of lipid-related features.

(legend continued on next page)

which associates with genes significantly enriched in oxidative phosphorylation (OXPHOS) and β-oxidation (WikiPathway 368 and WikiPathway 143), and *Lipid Granularity* in the cytoplasm, which associates with genes involved in fatty acid oxidation, mitochondrial long-chain fatty acid β-oxidation, and the TCA cycle. Finally, correlation features, which capture the overlap between lipid droplets, mitochondria, and AGP, were enriched for cytoplasmic ribosomal proteins, genes involved in mitochondrial long-chain fatty acid β-oxidation, and genes involved in insulin signaling in human adipocytes (Figures 3B and S3A; Table S1).

In addition to examining genes connected to feature groups, we also explored morphological features connected to specific genes. We found that morphological signatures of *SCD*, *PLIN2*, *LIPE*, *GLUT4*, *TIMM22*, and *INSR* revealed their known cellular functions (Figure 3C and Table S2). For example, the expression of *TIMM22*, a mitochondrial membrane gene, was most strongly correlated with *Mito Texture*. Expression of the insulin receptor (*INSR*) most strongly correlated with *Lipid Intensity* features indicative of lipid accumulation. *PLIN2* and *GLUT4* showed the highest positive and negative correlations with *Lipid* and *AGP* features, respectively. Together, these data show that mechanistic information gained from LipocyteProfiler features is not limited to generic cellular organelles but reflects the transcriptional state of the cell and can be deployed to gain relevant mechanistic insights.

LipocyteProfiler identifies cellular processes affected by drug perturbations in adipocytes and hepatocytes

To investigate whether LipocyteProfiler can identify effects of drug perturbations on cellular profiles, we first compared subcutaneous and visceral adipocytes that had been stimulated with the β-adrenergic agonist isoproterenol (Figure 4A). Isoproterenol is known to induce lipolysis and increase mitochondrial energy dissipation.[42] We observed that visceral adipocytes responded to isoproterenol treatment by changes in *Lipid* and *Mito* features (Figure 4B; Tables S3A and S3B). More specifically, we observed that isoproterenol-treated visceral adipocytes were characterized by differences in mitochondrial *Texture* (Difference Variance, q = 4.4×10^{-2}), indicative of a less-smooth appearance of mitochondrial staining compared with DMSO-treated controls (Figure 4C). This suggests that isoproterenol treatment results in more hyperpolarized and fragmented mitochondria, which is a reported mechanism of norepinephrine-stimulated browning in adipocytes.[37] Isoproterenol-treated visceral adipocytes are further characterized by increased *Lipid* Difference Variance (q = 1.8×10^{-2}) and decreased area of large *Lipid* objects, i.e., decreased mean radius and area of large lipid droplets (q = 2.5×10^{-2}) (Figure 4D) as well as decreased *Lipid Granularity* across the full granularity size spectra, particularly at the smallest lipid-droplet sizes (Figure 4E). In fact, LipocyteProfiler core features highlight the importance of decreased lipid-droplet size and lipid intensity (Table S3B). This pattern suggests less overall

lipid content in isoproterenol-treated lipolytic visceral adipocytes. Finally, the phenotypic response following isoproterenol treatment was predominant in visceral adipocytes, as we did not observe a significant effect (FDR < 5%) in subcutaneous adipocytes (Figure S3B). Indeed, adrenergic induced lipolysis is observed to be higher in visceral than subcutaneous in overweight and obese individuals.[43,44]

To test LipocyteProfiler in cell types beyond adipocytes, we assayed the effects of oleic acid and metformin in primary human hepatocytes (PHH). Consistent with the finding that free fatty acid treatment induces lipid-droplet accumulation in PHH,[45] our results showed that treatment of PHH with oleic acid yielded predominantly *Lipid* feature changes in the cell (Figure 4F and Table S4), with a morphological profile indicative of increased lipid-droplet number (*LargeLipidObjects_Count*, q = 3.4×10^{-10}) and overall lipid content (*Cells_MeanIntensity_Lipid*, q = 1.5×10^{-5}) as well as differences in *Texture* (*Cells_Texture_Entropy_Lipid*, q = 1.2×10^{-8}; *Cells_Texture_AngularSecondMoment_Lipid*, q = 1.8×10^{-6}; Figure 4G). By contrast, treatment of PHH with metformin caused morphological and cellular changes that were spread across all channels (Figure 4H and Table S5), with a profile suggestive of smaller cells (*Cells_AreaShape_Area*, q = 2.0×10^{-11}; *Cells_AreaShape_MinorAxisLength*, q = 7.2×10^{-12}) with increased mitochondrial membrane potential (*Cells_MeanIntensity_Mito*, q = 8.9×10^{-4}), and mitochondrial heterogeneity (*Cells_Texture_AngularSecondMoment_Mito*, q = 7.6×10^{-6}; *Cells_Texture_Entropy_Mito*, q = 9.8×10^{-7}; *Cells_Texture_InfoMeas1_Mito*, q = 3.3×10^{-13}). Additionally, we observed reduced lipid content (*Cells_MeanIntensity_Lipid*, q = 9.0×10^{-7}), reduced lipid-droplet number (*LargeLipidObjects_Count*, q = 4.8×10^{-8}), and differences in *Texture* (*Cells_Texture_Entropy_Lipid*, q = 7.1×10^{-5}) (Figure 4I). This concerted effect of metformin on mitochondrial structure and function as well as lipid-related features is consistent with a less uniform appearance of the cytoskeleton, Golgi, and plasma membrane in metformin-treated hepatocytes compared with control (*Cells_Texture_Angular SecondMoment_AGP*, q = 1.9×10^{-8}, Figure 4I). Indeed, prolonged treatment with high doses of metformin leads to mitochondrial uncoupling, resulting in mitochondrial hyperpolarization and diminished lipid accumulation in PHH.[45–47] Together, these data demonstrate that morphological and cellular profiles of drug perturbation in lipocytes yield cellular signatures reflecting known biology and drug action in a single concerted snapshot of cell behavior.

Polygenic risk effects for insulin resistance affects lipid degradation in differentiated visceral adipocytes

Next, we used LipocyteProfiler to discover cellular programs of metabolic polygenic risk in adipocytes. For systematic profiling of AMSCs in the context of natural genetic variation (Table S6), we first assessed the effect of both technical and biological

---

(G) Oleic acid treatment in PHH affects lipid-related morphological features suggestive of increased lipid-droplet size and number. y axis shows LP units (normalized LP values across PHH data, see STAR Methods).

(H) Metformin treatment in PHH results in global changes affecting features across all channels.

(I) Metformin effect in hepatocytes is suggestive of increased mitochondrial activity, while lipid-droplet size and number are reduced. Metformin-treated hepatocytes are also smaller and show reduced cytoskeletal randomness. y axis shows LP units (normalized LP values across PHH data, see STAR Methods).
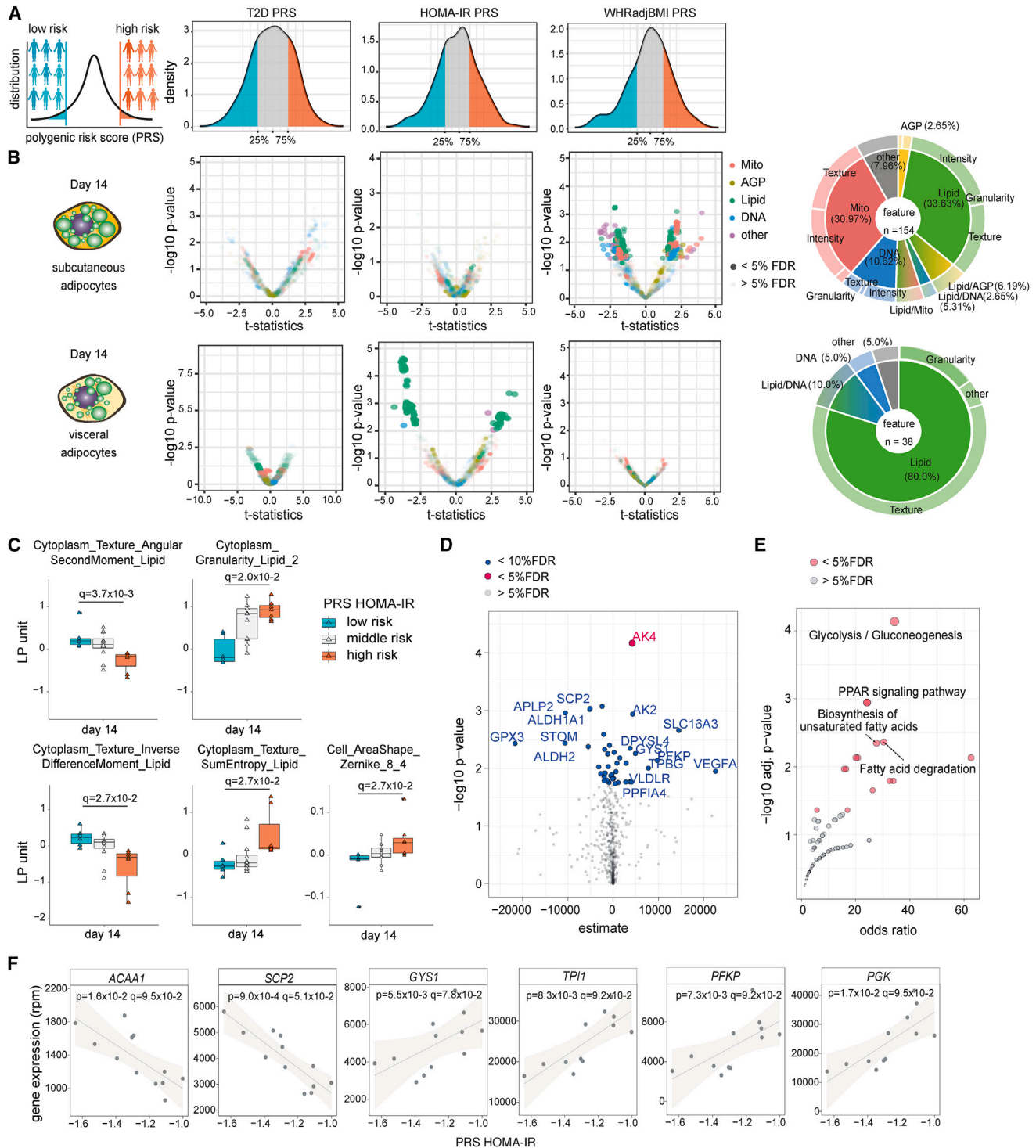
Figure 5. Polygenic risk effects for insulin resistance affect lipid degradation in differentiated visceral adipocytes

(A) Donors from the bottom and top 25 percentiles of genome-wide PRS for three T2D-related traits (HOMA-IR, T2D, WHRadjBMI) were selected to compare LipocyteProfiles across the time course of visceral and subcutaneous adipocyte differentiation.

(B) LipocyteProfiler applied to visceral and subcutaneous differentiating adipocytes reveals trait-specific polygenic effects on image-based cellular signatures for HOMA-IR in differentiated visceral AMSCs (day 14; largely *Lipid* features) and WHRadjBMI in subcutaneous adipocytes (day 14, largely *Mito* and *Lipid* features), but no effect for T2D. See also Figures S5A and S5D (days 0, 3, and 8).

(legend continued on next page)

variance on LipocyteProfiler features. To obtain a measure of batch-to-batch variance associated with our experimental setup, we differentiated hWAT, hBAT, and SGBS preadipocytes[48] in three independent experiments and found no significant batch effect (BEscore 0.0047, 0.0001, and 0.0003; Figure S4A). We also used a machine-learning-based classification model[49] to predict variables such as batch and cell type, based on the morphological profile. We show that the accuracy of predicting cell type is substantially higher than predicting batch (Figure S4A), indicating that our LipocyteProfiler framework can detect intrinsic versus extrinsic variance in our dataset with low batch effect and high accuracy. Second, we performed a variance component analysis across 65 donor-derived differentiating AMSCs to assess the contribution of intrinsic genetic variation compared with the contribution of other possible confounding factors such as batch, T2D status, age, sex, body mass index (BMI), cell density, and passage number. In total, we found that across all samples and batches, the largest contributor to feature variance was donor ID, accounting for 17.03% (interquartile range 11.45%–21.95%) of variance (Figure S4B). Other factors appeared to contribute only marginally to overall variance of the data, including extrinsic factors such as batch effect (6.02%, 3.94%–8.84%), plating density (3.75%, 1.55%–5.61%) and intrinsic factors such as sex (0.86%, 0.26%–2.44%), age (0.55%, 0.15%–1.39%), BMI (0.41%, 0.07%–1.33%), and T2D (0.19%, 0.03%–0.59%). These data suggest that LipocyteProfiler allows us to detect and distinguish interindividual genetic feature variation to a similar degree as reported for human induced pluripotent stem cells (iPSCs), where quantitative assays of cell morphology demonstrated a donor contribution to interindividual variation in the range of 8%–23%.[50] To account for the variable feature-specific contributions of batch, sex, age, and BMI to overall feature variance, we corrected for those covariables in our analyses. Together, these data suggest that LipocyteProfiler features can be used to study the effect of genetic contributions to morphological and cellular programs.

To ascertain the effect of polygenic risk for metabolic disease on cellular programs, we used the latest genome-wide association study (GWAS) summary statistics for T2D. We constructed individual genome-wide polygenic risk scores (PRSs) for three T2D-related traits that have been linked to adipose tissue: T2D,[51] insulin resistance by homeostasis measure assessment (HOMA-IR[52,53]), and waist-to-hip ratio adjusted for BMI (WHRadjBMI[54]). To evaluate whether HOMA-IR PRS effects are confounded by BMI, we compared the distribution of BMI between groups of high, medium, and low HOMA-IR PRS carriers and observed that HOMA-IR PRS appears to be largely independent of BMI (Kolmogorov-Smirnov tests: top 25% and bottom 25% p = 0.797, Figure S4C). Next, we selected donors from the bottom and top 25th percentiles of these genome-wide PRS distributions (referred to as low and high polygenic risk) and compared LipocyteProfiler features across the time course of visceral and subcutaneous adipocyte differentiation in high and low polygenic risk groups (Figures 5A, 5B, S5A, and S5D; Tables S7 and S8).

We found significant effects on image-based cellular signatures for HOMA-IR and WHRadjBMI, but no polygenic effect for T2D (Figures 5B, S5A, and S5D; Tables S7 and S8). More specifically, we observed an effect of HOMA-IR polygenic risk on cellular profiles at day 14 in visceral adipocytes (38 features, FDR < 5%, Figure 5B and Table S7A), indicating a spatiotemporal and depot-specific effect of polygenic risk for insulin resistance. The features that differed between the high and low HOMA-IR PRS carriers were mostly *Lipid* features (Figure 5B). Visceral adipocytes from high polygenic risk individuals showed increased *Lipid Granularity* (q = 2.0×10^{-2}), increased *Cytoplasm_Texture_SumEntropy_Lipid* (q = 2.7×10^{-2}), increased *Cells_AreaShape_Zernike_8_4* (q = 2.7×10^{-2}), decreased *Cytoplasm_Texture_InverseDifferenceMoment_Lipid* (q = 2.7×10^{-2}), and reduced *Cytoplasm_Texture_AngularSecondMoment_Lipid* (q = 3.7×10^{-3}) in the cytoplasm compared with low polygenic risk individuals (Figure 5C). The data further reveal that the pattern that contrasts between high and low HOMA-IR polygenic risk carriers is driven by lipid-informative LipocyteProfiler core features. Cellular signatures of high HOMA-IR polygenic risk carriers include core features that describe increased *Lipid Granularity*, increased *Lipid Radial Distribution* in the middle rings of the cell, and increased *Cell Area* (Tables S7B–S7D). These data indicate that visceral adipocytes from individuals with high compared with low polygenic risk for insulin resistance are characterized by a lipid-rich cellular profile, driven by key features informative for increased number of small to medium-sized lipid droplets, less homogeneous lipid-droplet distribution, and larger adipocytes, indicating excessive lipid accumulation in visceral adipocytes from individuals at high polygenic risk. Notably, the pattern that differentiates individuals at high and low polygenic risk recapitulates signatures that resemble an inhibition of lipolysis, as demonstrated by the inverse direction of effect in isoproterenol-stimulated visceral AMSCs shown in Figure 4. Furthermore, we observed that lower HOMA-IR PRS increases the number of small lipid droplets in visceral adipocytes, which are precisely the features affected in response to isoproterenol (Figures S5B and 4E). Together, these image-derived rich representations of cellular signatures describe a cellular program that is characterized by a metabolic switch toward lipid accumulation rather than lipolysis in visceral adipocytes derived from individuals at high polygenic risk for insulin resistance.

To further resolve the cellular program underlying HOMA-IR PRSs in visceral adipocytes and ascertain the effects of polygenic risk for HOMA-IR on gene expression, we integrated image-based information from LipocyteProfiler with RNA-seq data from the same donor-derived samples. Looking at mRNA levels for 512 genes known to be involved in adipocyte differentiation and

(C) HOMA-IR polygenic risk in visceral AMSCs manifested in altered lipid texture, lipid granularity, and cell shape features, resembling an inhibition of lipolysis. y axis shows LP units (normalized LP values across eight batches, see STAR Methods). See also Figure 4B (isoproterenol stimulation).

(D) Linear regression of gene expression levels of 512 genes known to be involved in adipocyte function with HOMA-IR PRS.

(E) Pathway enrichment analysis of genes that correlate with HOMA-IR PRSs (FDR < 10%) in visceral adipocytes highlight biological processes related to glucose metabolism, fatty acid transport, degradation, and lipolysis (KEGG pathways 2019).

(F) Representative genes that associate with HOMA-IR PRS in visceral adipocytes.

function (gene set enrichment analysis hallmark gene sets for adipogenesis, fatty acid metabolism, and glycolysis[55,56]), we identified 51 genes under the polygenic control of HOMA-IR (FDR < 10%) in fully differentiated visceral adipocytes (Figure 5D and Table S9). Genes correlating with the HOMA-IR PRS were enriched for biological processes related to glucose metabolism, fatty acid transport, degradation, and lipolysis (Figure 5E and Table S10). Negatively correlated genes include *ACAA1* (p = 1.6×10^{-2}, q = 9.5×10^{-2}) and *SCP2* (p = 9.0×10^{-4}, q = 5.1×10^{-2}) (Figure 5F), consistent with an inhibition of lipolysis and lipid degradation in visceral adipocytes from individuals at high polygenic risk for HOMA-IR. Positively correlated genes include *GYS1*, which is a regulator of glycogen biosynthesis shown to causally link glycogen metabolism to lipid-droplet formation in brown adipocytes[57] (p = 5.5×10^{-3}, q = 7.8×10^{-2}, Figure 5F). Additionally, multiple critical enzymes of the glycolysis pathway (*TPI1* [q = 9.2×10^{-2}], *PFKP* [q = 9.2×10^{-2}], *PGK* [q = 9.5×10^{-2}], Figure 5F), and marker genes of energy metabolism (*AK2* and *AK4*; Figure S5C) are positively correlated with HOMA-IR PRS, suggesting a metabolic switch from lipolytic degradation of triglycerides to glycolytic activity. Although a causal link between visceral adipose mass and insulin resistance has been widely observed,[58] the mechanism behind this observation is not understood. Together, orthogonal evidence from both high-content image- and RNA-based profiling experiments in subcutaneous and visceral AMSCs suggests that individuals with high polygenic risk for HOMA-IR are characterized by blocking lipid degradation in visceral adipocytes.

Polygenic risk for lipodystrophy-like phenotype manifests in cellular programs indicating reduced lipid accumulation capacity in subcutaneous adipocytes

To resolve polygenic effects on adipocyte cellular programs beyond heterogeneous T2D and insulin resistance traits, we used the clinically informed process-specific partitioned PRS of lipodystrophy,[59] and tested for association of the lipodystrophy-like PRS and LipocyteProfiler features throughout adipocyte differentiation (linear regression adjusted for BMI, age, sex, and principal component 1 [PC1], FDR < 5%; Table S11 and Figure 6A). The lipodystrophy PRS was constructed based on 20 T2D-associated loci that were grouped together as having similar associations with a lipodystrophy-like phenotype, signifying insulin resistance with a lower BMI[59] (Figure 6A). We found that polygenic risk of lipodystrophy associates with distinctive features in the *Mito*, *AGP*, and *Lipid* categories in subcutaneous AMSCs at day 8 and day 14 of differentiation, whereas increased lipodystrophy PRS associates primarily with *Lipid* features in visceral adipocytes at nominal significance (Figures 6B–6D and S6A; Table S11A). This highlights a depot- and spatiotemporal-dependent effect of polygenic risk on cellular profiles captured with LipocyteProfiler. Using the LipocyteProfiler core feature set, we identified *Mito Intensity*, *Texture*, and *Granularity* features, *AGP Granularity* features, and *Lipid Intensity* features to be most informative for driving the lipodystrophy PRS cellular process in subcutaneous adipocytes (Table S11B). More specifically, the profiles that associate with lipodystrophy polygenic risk include core features informative for increased mitochondrial membrane potential (e.g., *Cells_Intensity_Integrated_Inten-*

sity_Mito q = 3.4×10^{-2}; *Cells_Intensity_Mean Intensity_Mito* q = 3.4×10^{-2}; Table S11B), changes to the actin cytoskeleton indicating decreased cortical actin at the plasma membrane (e.g., *Cells_RadialDistribution_FracAtD_AGP* ring 2 of 4 q = 3.4×10^{-2} and 3 of 4 q = 3.4×10^{-2}; Figure S6B and Table S11B), and decreased lipid accumulation in subcutaneous adipocytes (e.g., *Cells_RadialDistribution_RadialCV_Lipid_4of4* q = 3.4×10^{-2}, *Cells_Texture_DifferenceEntropy_Lipid_10_00* q = 3.4×10^{-2}; Table S11B). Strikingly, representative images of subcutaneous adipocytes derived from individuals at the tail ends of lipodystrophy PRS (high risk [25th percentiles] compared with low risk [bottom 25th percentiles]) confirm that adipocytes from high PRS carriers have increased mitochondrial stain intensity—indicating higher mitochondrial membrane potential[60]—accompanied by smaller lipid droplets on average compared with adipocytes from individuals with low PRS (Figure 6D). We also note that CRISPR-Cas9-mediated knockout of the monogenic familial partial lipodystrophy gene *PLIN1* maps to features informative for decreased number of medium- and large-sized lipid droplets (Figure 1H), matching the polygenic risk effect. To assess whether the identified cellular changes underlying lipodystrophy polygenic risk resemble cellular drivers of monogenic forms of lipodystrophy, we next correlated expression of marker genes of monogenic familial partial lipodystrophy syndromes (*PPARG*, *LIPE*, *PLIN1*, *AKT2*, *CIDEC*, *LMNA*, and *ZMPSTE24*) with LipocyteProfiler features across subcutaneous adipocytes from 26 individuals. We found similar cellular signatures between profiles from monogenic lipodystrophy-associated genes and the polygenic lipodystrophy profile, with high effect sizes of *Mito* and *AGP* features (Figure S6C). These results suggest that polygenic and monogenic forms of lipodystrophy converge on similar cellular mechanisms involving increased mitochondrial activity and decreased lipid accumulation in subcutaneous adipocytes from high PRS donors. This finding is consistent with the fact that different monogenic forms of lipodystrophy showed similar consequences on mitochondrial OXPHOS in patient samples.[61]

To further resolve the cellular pathways of lipodystrophy polygenic risk that could underlie the morphological signature in subcutaneous adipocytes, we created a network of genes linked to features identified to be under the control of lipodystrophy polygenic risk. This analysis identified 23 genes that had ten or more connections to features derived from the lipodystrophy PRS LipocyteProfiler (FDR < 0.1%, Figure 6E). Sixteen of those genes are significantly (FDR < 10%) correlated with the lipodystrophy PRS (Figure S6D). For example, we found *EHHADH* (a marker gene of peroxisomal β-oxidation) and *NFATC3* (a gene involved in mitochondrial fragmentation and previously linked to a lipodystrophic phenotype in mice[62]) to be positively correlated with increased polygenic risk (q < 0.1 in both cases; Figure S6D), suggesting that gene networks identified through LipocyteProfiler signatures recapitulate mechanisms of polygenic risk and that LipocyteProfiler can be used to identify molecular mechanisms of disease risk.

Together, these data map aggregated polygenic risk for a lipodystrophy-like phenotype onto cellular programs characterized by increased mitochondrial activity and decreased lipid accumulation in subcutaneous adipocytes, which is consistent with the
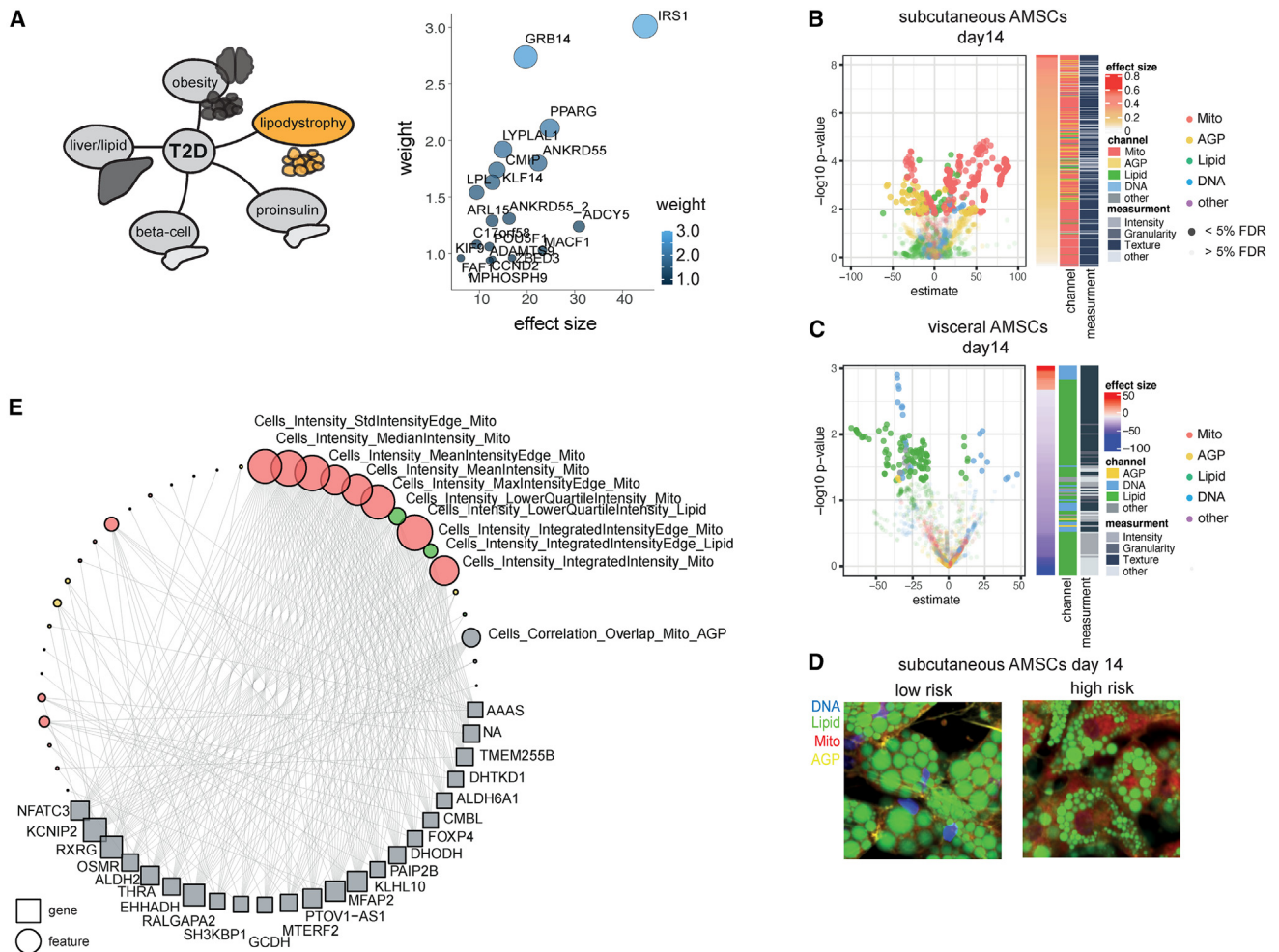
Figure 6. Polygenic risk for lipodystrophy-like phenotype manifests in cellular programs that indicate increased mitochondrial activity, reduced actin cytoskeleton remodeling, and reduced lipid accumulation capacity in subcutaneous adipocytes

(A) Schematic of T2D process-specific PRS (left panel). Lipodystrophy-specific PRS consists of 20 T2D-associated loci contributing to polygenic risk for a lipodystrophy-like phenotype.[59] y axis: weights of individual loci; x axis: effect size of individual loci contributing to polygenic risk for a lipodystrophy-like phenotype.

(B–D) Depot-specific effects on LipocyteProfiles in AMSCs at day 14 are under the polygenic control of the lipodystrophy cluster with a mitochondrial and AGP-driven profile in subcutaneous AMSCs (B), whereas in visceral AMSCs mostly *Lipid* features were associated with increased polygenic risk (C). See also Figure S6A (days 0, 3, and 8). Computationally averaged images of subcutaneous AMSCs from low- and high-risk allele carriers for lipodystrophy PRS show higher mitochondrial intensity, reduced cortical actin, and reduced lipid-droplet size in high-risk carriers (D).

(E) Gene-feature connections for lipodystrophy PRS-mediated differential features are enriched for Mitochondrial Intensity features informative for mitochondrial membrane potential in subcutaneous AMSCs at day 14 (FDR < 0.1%). See also Figure S6D.

notion that limited peripheral storage capacity of adipose tissue underlies polygenic lipodystrophy.[63]

Allele-specific effect of the *2p23.3* lipodystrophy-like locus on mitochondrial fragmentation and lipid accumulation in visceral adipocytes

To confirm that LipocyteProfiler can link an individual genetic risk locus to meaningful cellular profiles in visceral adipocytes, we investigated a locus on chromosome 2, spanning the *DNMT3A* gene at location *2p23.3*, which is one out of the 20 lipodystrophy process-specific risk loci included in the lipodystrophy PRS analyses. The *2p23.3* metabolic risk haplotype (minor allele fre-

quency of 0.35 in 1000 Genomes Phase 3 combined populations) is associated with a higher risk for T2D and WHRadjBMI (Figure 7A). To map the *2p23.3* metabolic risk locus to cellular functions, we compared LipocyteProfiler features of subcutaneous and visceral AMSCs from risk and non-risk haplotype carriers at three time points during adipocyte differentiation: before (day 0), early (day3), and terminal (day 14) differentiation (Figure 7B). In visceral AMSCs, we identified 92 and 23 core features that are significantly different between haplotypes at day 3 and day 14 of differentiation, respectively (Figure 7C and Table S12). At day 3, 70% of significantly different image-based features are mitochondrial, and on day 14, 80% of differential
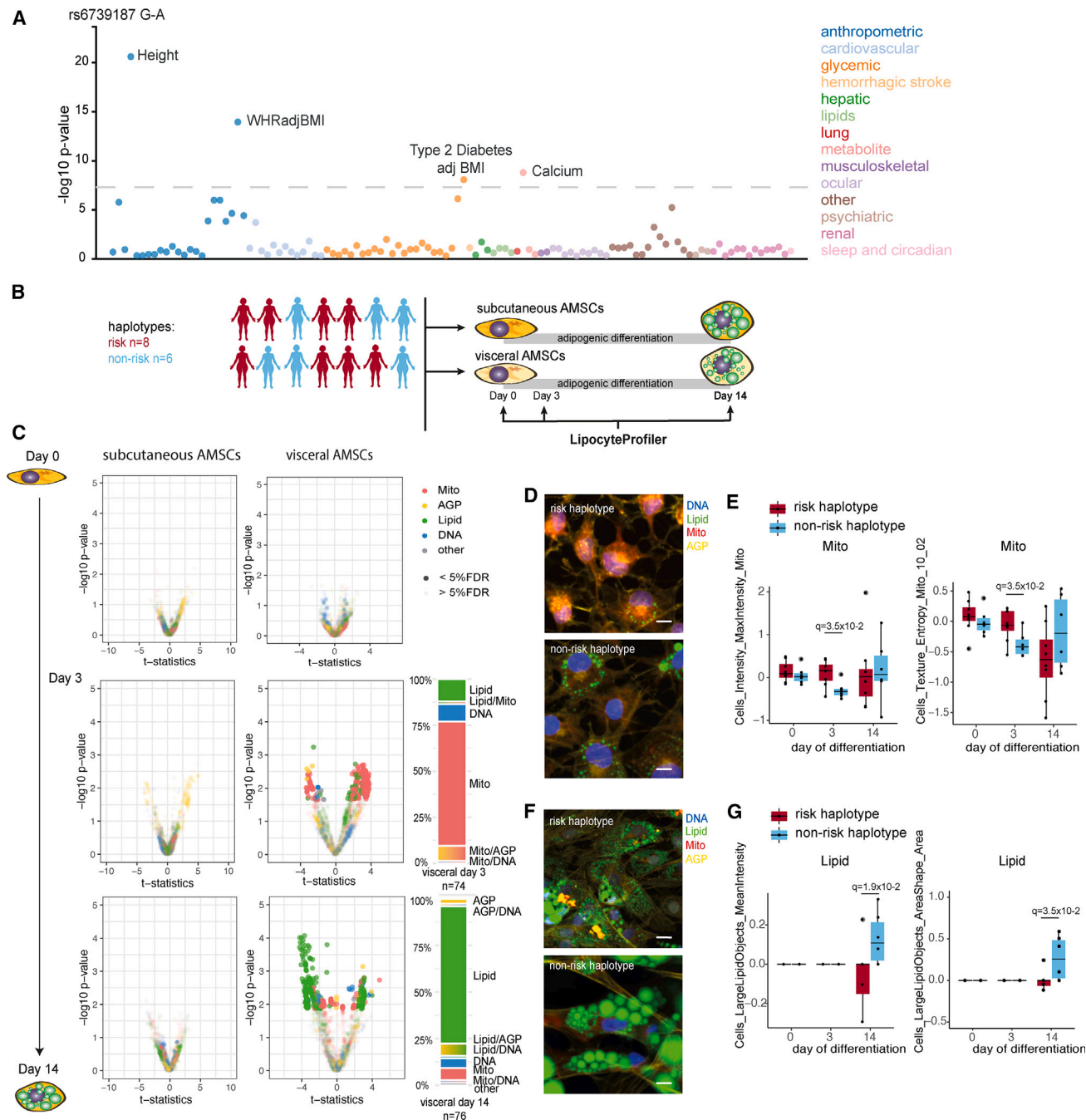
Figure 7. *2p23.3* lipodystrophy-like locus effect on mitochondrial fragmentation and lipid accumulation in visceral adipocytes

(A) PheWAS[66] at the *2q23.3* risk locus shows associations with height, WHRadjBMI, T2D, and Calcium.

(B) LipocyteProfiler was performed in subcutaneous and visceral AMSCs of eight risk and six non-risk haplotype carriers across adipocyte differentiation (days 0, 3, and 14).

(C) In visceral AMSCs, 74 and 76 features were different between haplotypes at day 3 and day 14 of differentiation, respectively, with 70% of differential features at day 3 being mitochondrial and 80% lipid-related at day 14.

(D) Representative images of visceral AMSCs from risk (top) and non-risk (bottom) haplotype at day 3 of differentiation stained using LipocytePainting. Scale bars, 10 μm.

(E) *Mito MaxIntensity* and *Mito Texture Entropy* were higher at day 3 of differentiation in visceral AMSCs from six risk haplotype carriers, suggesting more fragmented and higher mitochondrial membrane potential. y axis shows LP units (normalized LP values across eight batches, see STAR Methods).

(legend continued on next page)

features are lipid-related. These findings suggest that the *2p23.3* locus is associated with a mitochondrial function phenotype during early differentiation, which then progress to altered lipid-droplet formation in mature visceral adipocytes. Representative microscopic images from day 3 of differentiation show higher mitochondrial stain intensities in risk haplotype carriers (Figure 7D). The top-scoring, most differential mitochondrial features (*Cells_MaxIntensity_Mito* q = 3.5 × 10^{-2}, *Cells_Texture_Entropy_Mito* q = 3.5 × 10^{-2}, and *Cytoplasm_Granularity_7_Mito* q = 3.8 × 10^{-2}; Figures 7E and S7A) are increased in metabolic risk carriers, suggestive of less tubular mitochondria with increased mitochondrial membrane potential and altered function. At day 14 of differentiation, AMSCs from metabolic risk haplotype carriers show smaller lipid droplets in representative microscopic images (Figure 7F). More specifically, we observed that risk haplotype carriers have decreased *Lipid Intensity* (q = 1.9 × 10^{-2}; Figure 7G) in the cell and a smaller area of *large Lipid objects* (*LargeLipidobjects_AreaShape* q = 3.5 × 10^{-2}; Figure 7G), suggesting a lipid phenotype characterized by reduced lipid-droplet stabilization and/or formation. Distinct core features drive the genetic effect in visceral adipocytes at day 3, including *Mito Texture* (e.g., *DifferenceVariance* and *Entropy*) and at day 14 *Lipid Texture* features (Table S12A), highlighting cellular processes. This profile is associated with increased mature adipocyte diameter estimates (Figure 2) and suggests that risk haplotype carriers have a cellular profile that is consistent with visceral WAT hypertrophy. We further note that our findings in human adipocytes are corroborated by organismal perturbation of the candidate effector transcript *DNMT3A* in mice, where deletion of *Dnmt3a* results in changes of whole-body fat mass (Figure S7B)[64] and protects from high-fat-diet-induced insulin resistance, which is mainly attributed to actions in visceral adipose tissue.[65] Together, these data demonstrate that LipocyteProfiler captures complex cellular phenotypes associated with genetic risk for cardiometabolic diseases and traits and allows the effective resolution of spatial-temporal context of action. With LipocyteProfiler, we generated a resource that enables unbiased mechanistic interrogation of the hundreds of cardiometabolic disease loci with unknown functions. We have provided all data and software as open-access and open-source for the community.

DISCUSSION

We present a novel high-content image-based profiling framework, LipocyteProfiler, for enabling the identification of causal relationships between natural genetic variation, effect of drugs, and physiologically relevant stimulations, and the identification of effector genes with cellular programs in the context of cardiometabolic disease. We provide proof-of-principle results showcasing that we can link natural genetic variation to distinct morphological and cellular profiles using LipocyteProfiler-based deep phenotypic

profiles generated in primary AMSCs with a given genetic background. This demonstrates that LipocyteProfiler is useful for unraveling disease-relevant complex cellular programs beyond hypothesis-driven cell-based readouts alone. We show that the information gained from LipocyteProfiler can report on both physiological and pathological states of the cell and identify cellular traits underlying cell-state transitions, providing a controlled toolkit to interrogate dynamic rather than static programs. Using LipocyteProfiler in defined cell states, we can robustly detect subtle phenotypic differences driven by drug treatment, genetic perturbation, and natural genetic variation. Our ability to detect these subtle changes might be a consequence of cell traits capturing the downstream manifestations of genomic, transcriptional, and proteomic effects. We show that polygenic risk for metabolic traits converges into discrete pathways and mechanisms. LipocyteProfiler elucidates morphological and cellular signatures underlying differential polygenic metabolic risk specific to distinct adipose depots, metabolic traits, and cell-developmental time points. For example, we observed polygenic effects on lipid degradation in visceral adipocytes in the context of insulin resistance, and mitochondrial activity and cytoskeleton remodeling in subcutaneous adipocytes under the control of lipodystrophy-specific polygenic contributors to T2D risk. We note that the mitochondrial and actin cytoskeleton informative cellular programs which associate with a lipodystrophy-like phenotype show similarities to morphological signatures associated with genome-wide polygenic risk for WHRadjBMI, a proxy of unfavorable fat distribution. Future work using other adiposity PRSs such as described in Martin et al.[67] will help to identify genetic drivers of cardiometabolic disease and further deconvolve the cellular programs underlying favorable und unfavorable adiposity.

LipocyteProfiler enables scalable, unbiased, mechanistic interrogation of metabolic disease loci whose functions remain unknown. By linking image-based profiles to transcriptional states, we provide a rich resource of gene-cellular trait connections that relate image-based features to biological processes. We envision that LipocyteProfiler-generated quantitative, high-dimensional representations of morphological and cellular features will complement the palette of omics-based profiling readouts. Combined with forward and reverse genetic screens, this can link genetic perturbations to cellular programs in lipid-accumulating cells. We also note that LipocyteProfiler may generate a suitably complex readout to contribute to ongoing endeavors in the community to improve differentiation protocols of iPSCs and discover cellular programs underlying genetic perturbations in high-throughput genetic screens. Moreover, we expect that the power to identify genetic drivers for metabolic diseases will be demonstrated using a plethora of univariate and multivariate genome-wide polygenic scores to resolve the molecular heterogeneities of T2D and other cardiometabolic traits. Finally, we expect that, with increased sample sizes, our approach will help to pave the way to map cellular quantitative trait loci in

(F) Representative images of visceral AMSCs from risk (top) and non-risk (bottom) haplotype at day 14 of differentiation stained using LipocytePainting. Scale bars, 10 μm.
(G) *LargeLipidObject MedianIntensity* was lower and *Lipid Texture AngularSecondMoment* was higher at day 14 of differentiation in visceral AMSCs from six risk haplotype carriers, suggesting a perturbed lipid phenotype characterized by reduced lipid-droplet stabilization and/or formation. y axis shows LP units (normalized LP values across eight batches, see STAR Methods).

population-scale image-based profiling endeavors (GWAS-in-a-dish) to link common genetic risk variation to lipocyte phenotypes and accelerate therapeutic pathway discoveries. Our disease-oriented LipocyteProfiler image-based profiling tool can be modified by swapping or adding different disease-relevant dyes or antibodies of interest and could be applied to disease-relevant models for any disease of interest.

Limitations of the study

A primary limitation in the current study is the low sample size to link genetic variants to cellular and morphological processes, and as such we were not able to stratify by sex or other covariates. Findings presented here in our proof-of principle study need to be replicated in larger population-scale experiments in the future, which will help to evaluate reproducibility of our results and evaluate sex-specific polygenic risk effects in the context of cardiometabolic traits. We further acknowledge that the AMSCs are derived from patients undergoing abdominal laparoscopic surgery, and as such the BMI distribution of the patient cohort is skewed to high BMI (mean $49.34 \pm$ SD 11.28).

STAR★METHODS

Detailed methods are provided in the online version of this paper and include the following:

- KEY RESOURCES TABLE
- RESOURCE AVAILABILITY
  - Lead contact
  - Materials availability
  - Data and code availability
- EXPERIMENTAL MODEL AND SUBJECT DETAILS
  - Human primary AMSC isolation/abdominal laparoscopy cohort–Munich obesity BioBank/MOBB
  - Differentiation of human AMSCs
  - Primary human hepatocyte culture
  - MGB Biobank cohort
- METHOD DETAILS
  - LipocytePainting
  - Staining and microscopy of actin-cytoskeleton in subcutaneous AMSCs
  - Isolation and adipocyte diameter determination of floating mature adipocytes
  - CRISPR-Cas9-mediated knockout of adipocyte marker genes
- QUANTIFICATION AND STATISTICAL DETAILS
  - LipocyteProfiling
  - LipocyteProfiler feature reduction using ARACNE
  - Generating of average cells
  - RNA-seq
  - Gene expression and LipocyteProfiler feature network
  - Quality control of genotyping data
  - Constructing PRSs

SUPPLEMENTAL INFORMATION

Supplemental information can be found online at https://doi.org/10.1016/j.xgen.2023.100346.

INCLUSION AND DIVERSITY

We support inclusive, diverse, and equitable conduct of research.

REFERENCES

1. Feng, Y., Mitchison, T.J., Bender, A., Young, D.W., and Tallarico, J.A. (2009). Multi-parameter phenotypic profiling: using cellular effects to characterize small-molecule compounds. Nat. Rev. Drug Discov. *8*, 567–578. https://doi.org/10.1038/nrd2876.

2. Green, R.A., Kao, H.-L., Audhya, A., Arur, S., Mayers, J.R., Fridolfsson, H.N., Schulman, M., Schloissnig, S., Niessen, S., Laband, K., et al. (2011). A high-resolution C. elegans essential gene network based on phenotypic profiling of a complex tissue. Cell *145*, 470–482. https://doi.org/10.1016/j.cell.2011.03.037.

3. Hughes, R.E., Elliott, R.J.R., Dawson, J.C., and Carragher, N.O. (2021). High-content phenotypic and pathway profiling to advance drug discovery in diseases of unmet need. Cell Chem. Biol. 28, 338–355. https://doi.org/10.1016/j.chembiol.2021.02.015.

4. Neumann, B., Walter, T., Hériché, J.K., Bulkescher, J., Erfle, H., Conrad, C., Rogers, P., Poser, I., Held, M., Liebel, U., et al. (2010). Phenotypic profiling of the human genome by time-lapse microscopy reveals cell division genes. Nature 464, 721–727. https://doi.org/10.1038/nature08869.

5. Bray, M.-A., Singh, S., Han, H., Davis, C.T., Borgeson, B., Hartland, C., Kost-Alimova, M., Gustafsdottir, S.M., Gibson, C.C., and Carpenter, A.E. (2016). Cell Painting, a high-content image-based assay for morphological profiling using multiplexed fluorescent dyes. Nat. Protoc. 11, 1757–1774. https://doi.org/10.1038/nprot.2016.105.

6. Kepiro, M., Varkuti, B.H., and Davis, R.L. (2018). High content, phenotypic assays and screens for compounds modulating cellular processes in primary neurons. Methods Enzymol. 610, 219–250. https://doi.org/10.1016/bs.mie.2018.09.021.

7. Scheeder, C., Heigwer, F., and Boutros, M. (2018). Machine learning and image-based profiling in drug discovery. Curr. Opin. Struct. Biol. 10, 43–52. https://doi.org/10.1016/j.coisb.2018.05.004.

8. Simm, J., Klambauer, G., Arany, A., Steijaert, M., Wegner, J.K., Gustin, E., Chupakhin, V., Chong, Y.T., Vialard, J., Buijnsters, P., et al. (2018). Repurposing high-throughput image assays enables biological activity prediction for drug discovery. Cell Chem. Biol. 25, 611–618.e3. https://doi.org/10.1016/j.chembiol.2018.01.015.

9. Wawer, M.J., Li, K., Gustafsdottir, S.M., Ljosa, V., Bodycombe, N.E., Marton, M.A., Sokolnicki, K.L., Bray, M.-A., Kemp, M.M., Winchester, E., et al. (2014). Toward performance-diverse small-molecule libraries for cell-based phenotypic screening using multiplexed high-dimensional profiling. Proc. Natl. Acad. Sci. USA 111, 10911–10916. https://doi.org/10.1073/pnas.1410933111.

10. Rohban, M.H., Singh, S., Wu, X., Berthet, J.B., Bray, M.-A., Shrestha, Y., Varelas, X., Boehm, J.S., and Carpenter, A.E. (2017). Systematic morphological profiling of human gene and allele function via Cell Painting. Elife 6, e24060. https://doi.org/10.7554/eLife.24060.

11. Olzmann, J.A., and Carvalho, P. (2019). Dynamics and functions of lipid droplets. Nat. Rev. Mol. Cell Biol. 20, 137–155. https://doi.org/10.1038/s41580-018-0085-z.

12. Grandl, M., and Schmitz, G. (2010). Fluorescent high-content imaging allows the discrimination and quantitation of E-LDL-induced lipid droplets and Ox-LDL-generated phospholipidosis in human macrophages. Cytometry A. 77, 231–242.

13. Liu, L., Zhang, K., Sandoval, H., Yamamoto, S., Jaiswal, M., Sanz, E., Li, Z., Hui, J., Graham, B.H., Quintana, A., and Bellen, H.J. (2015). Glial lipid droplets and ROS induced by mitochondrial defects promote neurodegeneration. Cell 160, 177–190. https://doi.org/10.1016/j.cell.2014.12.019.

14. Robichaud, S., Fairman, G., Vijithakumar, V., Mak, E., Cook, D.P., Pelletier, A.R., Huard, S., Vanderhyden, B.C., Figeys, D., Lavallée-Adam, M., et al. (2021). Identification of novel lipid droplet factors that regulate lipophagy and cholesterol efflux in macrophage foam cells. Autophagy 17, 3671–3689. https://doi.org/10.1080/15548627.2021.1886839.

15. Wang, H., Quiroga, A.D., and Lehner, R. (2013a). Analysis of lipid droplets in hepatocytes. Methods Cell Biol. 116, 107–127. https://doi.org/10.1016/b978-0-12-408051-5.00007-3.

16. Cruz, A.L.S., Barreto, E.d.A., Fazolini, N.P.B., Viola, J.P.B., and Bozza, P.T. (2020). Lipid droplets: platforms with multiple functions in cancer hallmarks. Cell Death Dis. 11, 105. https://doi.org/10.1038/s41419-020-2297-3.

17. Hershey, B.J., Vazzana, R., Joppi, D.L., and Havas, K.M. (2019). Lipid droplets define a sub-population of breast cancer stem cells. J. Clin. Med. 9, 87. https://doi.org/10.3390/jcm9010087.

18. Prats, C., Donsmark, M., Qvortrup, K., Londos, C., Sztalryd, C., Holm, C., Galbo, H., and Ploug, T. (2006). Decrease in intramuscular lipid droplets and translocation of HSL in response to muscle contraction and epinephrine. J. Lipid Res. 47, 2392–2399. https://doi.org/10.1194/jlr.M600247-JLR200.

19. Wang, Z., Jiang, T., Li, J., Proctor, G., McManaman, J.L., Lucia, S., Chua, S., and Levi, M. (2005). Regulation of renal lipid metabolism, lipid accumulation, and glomerulosclerosis in FVBdb/db mice with type 2 diabetes. Diabetes 54, 2328–2335. https://doi.org/10.2337/diabetes.54.8.2328.

20. Weinert, S., Poitz, D.M., Auffermann-Gretzinger, S., Eger, L., Herold, J., Medunjanin, S., Schmeisser, A., Strasser, R.H., and Braun-Dullaeus, R.C. (2013). The lysosomal transfer of LDL/cholesterol from macrophages into vascular smooth muscle cells induces their phenotypic alteration. Cardiovasc. Res. 97, 544–552. https://doi.org/10.1093/cvr/cvs367.

21. Xu, S., Zhang, X., and Liu, P. (2018). Lipid droplet proteins and metabolic diseases. Biochim. Biophys. Acta, Mol. Basis Dis. 1864, 1968–1983. https://doi.org/10.1016/j.bbadis.2017.07.019.

22. Bray, M.-A., and Carpenter, A. (2017). Advanced assay development guidelines for image-based high content screening and analysis. In Assay Guidance Manual, S. Markossian, G.S. Sittampalam, A. Grossman, K. Brimacombe, M. Arkin, D. Auld, C.P. Austin, J. Baell, J.M.M. Caaveiro, and T.D.Y. Chung, et al., eds. (Eli Lilly & Company and the National Center for Advancing Translational Sciences).

23. Caicedo, J.C., Cooper, S., Heigwer, F., Warchal, S., Qiu, P., Molnar, C., Vasilevich, A.S., Barry, J.D., Bansal, H.S., Kraus, O., et al. (2017). Data-analysis strategies for image-based cell profiling. Nat. Methods 14, 849–863. https://doi.org/10.1038/nmeth.4397.

24. Gustafsdottir, S.M., Ljosa, V., Sokolnicki, K.L., Anthony Wilson, J., Walpita, D., Kemp, M.M., Petri Seiler, K., Carrel, H.A., Golub, T.R., Schreiber, S.L., et al. (2013). Multiplex cytological profiling assay to measure diverse cellular states. PLoS One 8, e80999. https://doi.org/10.1371/journal.pone.0080999.

25. Butte, A.J., and Kohane, I.S. (1999). Mutual information relevance networks: functional genomic clustering using pairwise entropy measurements. Pac. Symp. Biocomput., 418–429. https://doi.org/10.1142/9789814447331_0040.

26. Lachmann, A., Giorgi, F.M., Lopez, G., and Califano, A. (2016). ARACNe-AP: gene network reverse engineering through adaptive partitioning inference of mutual information. Bioinformatics 32, 2233–2235. https://doi.org/10.1093/bioinformatics/btw216.

27. Li, Y., Liang, C., Wong, K.-C., Jin, K., and Zhang, Z. (2014). Inferring probabilistic miRNA-mRNA interaction signatures in cancers: a role-switch approach. Nucleic Acids Res. 42, e76. https://doi.org/10.1093/nar/gku182.

28. Tachmazidou, I., Süveges, D., Min, J.L., Ritchie, G.R.S., Steinberg, J., Walter, K., Iotchkova, V., Schwartzentruber, J., Huang, J., Memari, Y., et al. (2017). Whole-genome sequencing coupled to imputation discovers genetic signals for anthropometric traits. Am. J. Hum. Genet. 100, 865–884. https://doi.org/10.1016/j.ajhg.2017.04.014.

29. Xue, R., Lynes, M.D., Dreyfuss, J.M., Shamsi, F., Schulz, T.J., Zhang, H., Huang, T.L., Townsend, K.L., Li, Y., Takahashi, H., et al. (2015). Clonal analyses and gene profiling identify genetic biomarkers of the thermogenic potential of human brown and white preadipocytes. Nat. Med. 21, 760–768. https://doi.org/10.1038/nm.3881.

30. Kanzaki, M. (2006). Insulin receptor signals regulating GLUT4 translocation and actin dynamics. Endocr. J. 53, 267–293. https://doi.org/10.1507/endocrj.kr-65.

31. Cedikova, M., Kripnerová, M., Dvorakova, J., Pitule, P., Grundmanova, M., Babuska, V., Mullerova, D., and Kuncova, J. (2016). Mitochondria in white, Brown, and beige adipocytes. Stem Cell. Int. 2016, 6067349. https://doi.org/10.1155/2016/6067349.

32. Fei, W., Du, X., and Yang, H. (2011). Seipin, adipogenesis and lipid droplets. Trends Endocrinol. Metab. 22, 204–210. https://doi.org/10.1016/j.tem.2011.02.004.

33. Gandotra, S., Le Dour, C., Bottomley, W., Cervera, P., Giral, P., Reznik, Y., Charpentier, G., Auclair, M., Delépine, M., Barroso, I., et al. (2011). Perilipin deficiency and autosomal dominant partial lipodystrophy. N. Engl. J. Med. *364*, 740–748. https://doi.org/10.1056/NEJMoa1007487.

34. Shijun, L., Khan, R., Raza, S.H.A., Jieyun, H., Chugang, M., Kaster, N., Gong, C., Chunping, Z., Schreurs, N.M., and Linsen, Z. (2020). Function and characterization of the promoter region of perilipin 1 (PLIN1): roles of E2F1, PLAG1, C/EBPβ, and SMAD3 in bovine adipocytes. Genomics *112*, 2400–2409. https://doi.org/10.1016/j.ygeno.2020.01.012.

35. Brasaemle, D.L., Barber, T., Wolins, N.E., Serrero, G., Blanchette-Mackie, E.J., and Londos, C. (1997). Adipose differentiation-related protein is an ubiquitously expressed lipid storage droplet-associated protein. J. Lipid Res. *38*, 2249–2263.

36. Tsai, T.-H., Chen, E., Li, L., Saha, P., Lee, H.-J., Huang, L.-S., Shelness, G.S., Chan, L., and Chang, B.H.-J. (2017). The constitutive lipid droplet protein PLIN2 regulates autophagy in liver. Autophagy *13*, 1130–1144. https://doi.org/10.1080/15548627.2017.1319544.

37. Gao, A.W., and Houtkooper, R.H. (2014). Mitochondrial fission: firing up mitochondria in brown adipose tissue. EMBO J. *33*, 401–402. https://doi.org/10.1002/embj.201487798.

38. Qiu, P., Gentles, A.J., and Plevritis, S.K. (2011). Discovering biological progression underlying microarray samples. PLoS Comput. Biol. *7*, e1001123. https://doi.org/10.1371/journal.pcbi.1001123.

39. Baglioni, S., Cantini, G., Poli, G., Francalanci, M., Squecco, R., Di Franco, A., Borgogni, E., Frontera, S., Nesi, G., Liotta, F., et al. (2012). Functional differences in visceral and subcutaneous fat pads originate from differences in the adipose stem cell. PLoS One *7*, e36569. https://doi.org/10.1371/journal.pone.0036569.

40. Wang, Q.A., Tao, C., Gupta, R.K., and Scherer, P.E. (2013b). Tracking adipogenesis during white adipose tissue development, expansion and regeneration. Nat. Med. *19*, 1338–1344. https://doi.org/10.1038/nm.3324.

41. Kusminski, C.M., and Scherer, P.E. (2012). Mitochondrial dysfunction in white adipose tissue. Trends Endocrinol. Metabol. *23*, 435–443. https://doi.org/10.1016/j.tem.2012.06.004.

42. Miller, C.N., Yang, J.-Y., England, E., Yin, A., Baile, C.A., and Rayalam, S. (2015). Isoproterenol increases uncoupling, glycolysis, and markers of beiging in mature 3T3-L1 adipocytes. PLoS One *10*, e0138344. https://doi.org/10.1371/journal.pone.0138344.

43. Hoffstedt, J., Arner, P., Hellers, G., and Lönnqvist, F. (1997). Variation in adrenergic regulation of lipolysis between omental and subcutaneous adipocytes from obese and non-obese men. J. Lipid Res. *38*, 795–804.

44. Morigny, P., Boucher, J., Arner, P., and Langin, D. (2021). Lipid and glucose metabolism in white adipocytes: pathways, dysfunction and therapeutics. Nat. Rev. Endocrinol. *17*, 276–295. https://doi.org/10.1038/s41574-021-00471-8.

45. Liu, F., Wang, C., Zhang, L., Xu, Y., Jang, L., Gu, Y., Cao, X., Zhao, X., Ye, J., and Li, Q. (2014). Metformin prevents hepatic steatosis by regulating the expression of adipose differentiation-related protein. Int. J. Mol. Med. *33*, 51–58. https://doi.org/10.3892/ijmm.2013.1560.

46. Demine, S., Renard, P., and Arnould, T. (2019). Mitochondrial uncoupling: a key controller of biological processes in physiology and diseases. Cells *8*. https://doi.org/10.3390/cells8080795.

47. Forkink, M., Manjeri, G.R., Liemburg-Apers, D.C., Nibbeling, E., Blanchard, M., Wojtala, A., Smeitink, J.A.M., Wieckowski, M.R., Willems, P.H.G.M., and Koopman, W.J.H. (2014). Mitochondrial hyperpolarization during chronic complex I inhibition is sustained by low activity of complex II, III, IV and V. Biochim. Biophys. Acta *1837*, 1247–1256. https://doi.org/10.1016/j.bbabio.2014.04.008.

48. Fischer-Posovszky, P., Newell, F.S., Wabitsch, M., and Tornqvist, H.E. (2008). Human SGBS cells - a unique tool for studies of human fat cell biology. Obes. Facts *1*, 184–189. https://doi.org/10.1159/000145784.

49. Venables, W.N., and Ripley, B.D. (2002). Random and mixed effects. Modern Applied Statistics with S, 271–300. Springer.

50. Kilpinen, H., Goncalves, A., Leha, A., Afzal, V., Alasoo, K., Ashford, S., Bala, S., Bensaddek, D., Casale, F.P., Culley, O.J., et al. (2017). Common genetic variation drives molecular heterogeneity in human iPSCs. Nature *546*, 370–375. https://doi.org/10.1038/nature22403.

51. Mahajan, A., Taliun, D., Thurner, M., Robertson, N.R., Torres, J.M., Rayner, N.W., Payne, A.J., Steinthorsdottir, V., Scott, R.A., Grarup, N., et al. (2018). Fine-mapping type 2 diabetes loci to single-variant resolution using high-density imputation and islet-specific epigenome maps. Nat. Genet. *50*, 1505–1513. https://doi.org/10.1038/s41588-018-0241-6.

52. Dupuis, J., Langenberg, C., Prokopenko, I., Saxena, R., Soranzo, N., Jackson, A.U., Wheeler, E., Glazer, N.L., Bouatia-Naji, N., Gloyn, A.L., et al. (2010). New genetic loci implicated in fasting glucose homeostasis and their impact on type 2 diabetes risk. Nat. Genet. *42*, 105–116. https://doi.org/10.1038/ng.520.

53. Matthews, D.R., Hosker, J.P., Rudenski, A.S., Naylor, B.A., Treacher, D.F., and Turner, R.C. (1985). Homeostasis model assessment: insulin resistance and beta-cell function from fasting plasma glucose and insulin concentrations in man. Diabetologia *28*, 412–419. https://doi.org/10.1007/BF00280883.

54. Pulit, S.L., Stoneman, C., Morris, A.P., Wood, A.R., Glastonbury, C.A., Tyrrell, J., Yengo, L., Ferreira, T., Marouli, E., Ji, Y., et al. (2019). Meta-analysis of genome-wide association studies for body fat distribution in 694 649 individuals of European ancestry. Hum. Mol. Genet. *28*, 166–174. https://doi.org/10.1093/hmg/ddy327.

55. Mootha, V.K., Lindgren, C.M., Eriksson, K.-F., Subramanian, A., Sihag, S., Lehar, J., Puigserver, P., Carlsson, E., Ridderstråle, M., Laurila, E., et al. (2003). PGC-1α-responsive genes involved in oxidative phosphorylation are coordinately downregulated in human diabetes. Nat. Genet. *34*, 267–273. https://doi.org/10.1038/ng1180.

56. Subramanian, A., Tamayo, P., Mootha, V.K., Mukherjee, S., Ebert, B.L., Gillette, M.A., Paulovich, A., Pomeroy, S.L., Golub, T.R., Lander, E.S., and Mesirov, J.P. (2005). Gene set enrichment analysis: a knowledge-based approach for interpreting genome-wide expression profiles. Proc. Natl. Acad. Sci. USA *102*, 15545–15550. https://doi.org/10.1073/pnas.0506580102.

57. Mayeuf-Louchart, A., Lancel, S., Sebti, Y., Pourcet, B., Loyens, A., Delhaye, S., Duhem, C., Beauchamp, J., Ferri, L., Thorel, Q., et al. (2019). Glycogen dynamics drives lipid droplet biogenesis during Brown adipocyte differentiation. Cell Rep. *29*, 1410–1418.e6. https://doi.org/10.1016/j.celrep.2019.09.073.

58. Lebovitz, H.E., and Banerji, M.A. (2005). Point: visceral adiposity is causally related to insulin resistance. Diabetes Care *28*, 2322–2325. https://doi.org/10.2337/diacare.28.9.2322.

59. Udler, M.S., Kim, J., von Grotthuss, M., Bonàs-Guarch, S., Cole, J.B., Chiou, J., Anderson, C.D. on behalf of METASTROKE and the ISGC; Boehnke, M., Laakso, M., Atzmon, G., et al. (2018). Type 2 diabetes genetic loci informed by multi-trait associations point to disease mechanisms and subtypes: a soft clustering analysis. PLoS Med. *15*, e1002654. https://doi.org/10.1371/journal.pmed.1002654.

60. Xiao, B., Deng, X., Zhou, W., and Tan, E.-K. (2016). Flow cytometry-based assessment of mitophagy using MitoTracker. Front. Cell. Neurosci. *10*, 76. https://doi.org/10.3389/fncel.2016.00076.

61. Sleigh, A., Stears, A., Thackray, K., Watson, L., Gambineri, A., Nag, S., Campi, V.I., Schoenmakers, N., Brage, S., Carpenter, T.A., et al. (2012). Mitochondrial oxidative phosphorylation is impaired in patients with congenital lipodystrophy. J. Clin. Endocrinol. Metab. *97*, E438–E442. https://doi.org/10.1210/jc.2011-2587.

62. Hu, L., He, F., Huang, M., Peng, M., Zhou, Z., Liu, F., and Dai, Y.-S. (2018). NFATc3 deficiency reduces the classical activation of adipose tissue macrophages. J. Mol. Endocrinol. *61*, 79–89. https://doi.org/10.1530/JME-18-0070.

63. Lotta, L.A., Gulati, P., Day, F.R., Payne, F., Ongen, H., van de Bunt, M., Gaulton, K.J., Eicher, J.D., Sharp, S.J., Luan, J., et al. (2017). Integrative genomic analysis implicates limited peripheral adipose storage capacity

in the pathogenesis of human insulin resistance. Nat. Genet. *49*, 17–26. https://doi.org/10.1038/ng.3714.

64. Dickinson, M.E., Flenniken, A.M., Ji, X., Teboul, L., Wong, M.D., White, J.K., Meehan, T.F., Weninger, W.J., Westerberg, H., Adissu, H., et al. (2016). High-throughput discovery of novel developmental phenotypes. Nature *537*, 508–514. https://doi.org/10.1038/nature19356.

65. You, D., Nilsson, E., Tenen, D.E., Lyubetskaya, A., Lo, J.C., Jiang, R., Deng, J., Dawes, B.A., Vaag, A., Ling, C., et al. (2017). Dnmt3a is an epigenetic mediator of adipose insulin resistance. Elife *6*, e30766. https://doi.org/10.7554/eLife.30766.

66. Gagliano Taliun, S.A., VandeHaar, P., Boughton, A.P., Welch, R.P., Taliun, D., Schmidt, E.M., Zhou, W., Nielsen, J.B., Willer, C.J., Lee, S., et al. (2020). Exploring and visualizing large-scale genetic associations by using PheWeb. Nat. Genet. *52*, 550–552.

67. Martin, S., Cule, M., Basty, N., Tyrrell, J., Beaumont, R.N., Wood, A.R., Frayling, T.M., Sorokin, E., Whitcher, B., Liu, Y., et al. (2021). Genetic evidence for different adiposity phenotypes and their opposing influences on ectopic fat and risk of cardiometabolic disease. Diabetes *70*, 1843–1856. https://doi.org/10.2337/db21-0129.

68. Pinello, L., Canver, M.C., Hoban, M.D., Orkin, S.H., Kohn, D.B., Bauer, D.E., and Yuan, G.-C. (2016). Analyzing CRISPR genome-editing experiments with CRISPResso. Nat. Biotechnol. *34*, 695–697. https://doi.org/10.1038/nbt.3583.

69. Chang, C.C., Chow, C.C., Tellier, L.C., Vattikuti, S., Purcell, S.M., and Lee, J.J. (2015). Second-generation PLINK: rising to the challenge of larger and richer datasets. GigaScience *4*, 7. https://doi.org/10.1186/s13742-015-0047-8.

70. Delaneau, O., Zagury, J.-F., and Marchini, J. (2013). Improved whole-chromosome phasing for disease and population genetic studies. Nat. Methods *10*, 5–6. https://doi.org/10.1038/nmeth.2307.

71. Ge, T., Chen, C.-Y., Ni, Y., Feng, Y.-C.A., and Smoller, J.W. (2019). Polygenic prediction via Bayesian regression and continuous shrinkage priors. Nat. Commun. *10*, 1776. https://doi.org/10.1038/s41467-019-09718-5.

72. Vilhjálmsson, B.J., Yang, J., Finucane, H.K., Gusev, A., Lindström, S., Ripke, S., Genovese, G., Loh, P.-R., Bhatia, G., Do, R., et al. (2015). Modeling linkage disequilibrium increases accuracy of polygenic risk scores. Am. J. Hum. Genet. *97*, 576–592. https://doi.org/10.1016/j.ajhg.2015.09.001.

73. Dobin, A., Davis, C.A., Schlesinger, F., Drenkow, J., Zaleski, C., Jha, S., Batut, P., Chaisson, M., and Gingeras, T.R. (2013). STAR: ultrafast universal RNA-seq aligner. Bioinformatics *29*, 15–21. https://doi.org/10.1093/bioinformatics/bts635.

74. Love, M.I., Huber, W., and Anders, S. (2014). Moderated estimation of fold change and dispersion for RNA-seq data with DESeq2. Genome Biol. *15*, 550. https://doi.org/10.1186/s13059-014-0550-8.

75. Margolin, A.A., Nemenman, I., Basso, K., Wiggins, C., Stolovitzky, G., Dalla Favera, R., and Califano, A. (2006). ARACNE: an algorithm for the reconstruction of gene regulatory networks in a mammalian cellular context. BMC Bioinf. *7*, S7. https://doi.org/10.1186/1471-2105-7-S1-S7.

76. McInnes, L., Healy, J., Saul, N., and Großberger, L. (2018). UMAP: uniform manifold approximation and projection. J. Open Source Softw. *3*, 861. https://doi.org/10.21105/joss.00861.

77. Gu, Z., Eils, R., and Schlesner, M. (2016). Complex heatmaps reveal patterns and correlations in multidimensional genomic data. Bioinformatics *32*, 2847–2849. https://doi.org/10.1093/bioinformatics/btw313.

78. Akulenko, R., Merl, M., and Helms, V. (2016). BEclear: batch effect detection and adjustment in DNA methylation data. PLoS One *11*, e0159921. https://doi.org/10.1371/journal.pone.0159921.

79. Skurk, T., and Hauner, H. (2012). Primary culture of human adipocyte precursor cells: expansion and differentiation. Methods Mol. Biol. *806*, 215–226. https://doi.org/10.1007/978-1-61779-367-7_15.

80. Raajendiran, A., Ooi, G., Bayliss, J., O'Brien, P.E., Schittenhelm, R.B., Clark, A.K., Taylor, R.A., Rodeheffer, M.S., Burton, P.R., and Watt, M.J. (2019). Identification of metabolically distinct adipocyte progenitor cells in human adipose tissues. Cell Rep. *27*, 1528–1540.e7. https://doi.org/10.1016/j.celrep.2019.04.010.

81. Karlson, E.W., Boutin, N.T., Hoffnagle, A.G., and Allen, N.L. (2016). Building the Partners HealthCare Biobank at Partners personalized medicine: informed consent, return of research results, recruitment lessons and operational considerations. J. Personalized Med. *6*, 2. https://doi.org/10.3390/jpm6010002.

82. Yu, S., Liao, K.P., Shaw, S.Y., Gainer, V.S., Churchill, S.E., Szolovits, P., Murphy, S.N., Kohane, I.S., and Cai, T. (2015). Toward high-throughput phenotyping: unbiased automated feature extraction and selection from knowledge sources. J. Am. Med. Inf. Assoc. *22*, 993–1000. https://doi.org/10.1093/jamia/ocv034.

83. Fischer, B., Schöttl, T., Schempp, C., Fromme, T., Hauner, H., Klingenspor, M., and Skurk, T. (2015). Inverse relationship between body mass index and mitochondrial oxidative phosphorylation capacity in human subcutaneous adipocytes. Am. J. Physiol. Endocrinol. Metab. *309*, E380–E387. https://doi.org/10.1152/ajpendo.00524.2014.

84. Shalem, O., Sanjana, N.E., Hartenian, E., Shi, X., Scott, D.A., Mikkelson, T., Heckl, D., Ebert, B.L., Root, D.E., Doench, J.G., and Zhang, F. (2014). Genome-scale CRISPR-Cas9 knockout screening in human cells. Science *343*, 84–87. https://doi.org/10.1126/science.1247005.

85. Pedregosa, F., Varoquaux, G., Gramfort, A., Michel, V., Thirion, B., Grisel, O., Blondel, M., Prettenhofer, P., Weiss, R., Dubourg, V., et al. (2011). Scikit-learn: machine learning in Python. J. Mach. Learn. Res. *12*, 2825–2830.

86. Jang, I.S., Margolin, A., and Califano, A. (2013). hARACNe: improving the accuracy of regulatory model reverse engineering via higher-order data processing inequality tests. Interface Focus *3*, 20130011. https://doi.org/10.1098/rsfs.2013.0011.

87. Wang, X., Hripcsak, G., and Friedman, C. (2009). Characterizing environmental and phenotypic associations using information theory and electronic health records. BMC Bioinf. *10* (*Suppl 9*), S13. https://doi.org/10.1186/1471-2105-10-s9-s13.

88. Krueger, F. (2015). A Wrapper Tool Around Cutadapt and FastQC to Consistently Apply Quality and Adapter Trimming to FastQ Files (Babraham Institute).

89. Liao, Y., Smyth, G.K., and Shi, W. (2019). The R package Rsubread is easier, faster, cheaper and better for alignment and quantification of RNA sequencing reads. Nucleic Acids Res. *47*, e47. https://doi.org/10.1093/nar/gkz114.

90. Purcell, S., Neale, B., Todd-Brown, K., Thomas, L., Ferreira, M.A.R., Bender, D., Maller, J., Sklar, P., de Bakker, P.I.W., Daly, M.J., and Sham, P.C. (2007). PLINK: a tool set for whole-genome association and population-based linkage analyses. Am. J. Hum. Genet. *81*, 559–575. https://doi.org/10.1086/519795.

91. McCarthy, S., Das, S., Kretzschmar, W., Delaneau, O., Wood, A.R., Teumer, A., Kang, H.M., Fuchsberger, C., Danecek, P., Sharp, K., et al. (2016). A reference panel of 64,976 haplotypes for genotype imputation. Nat. Genet. *48*, 1279–1283. https://doi.org/10.1038/ng.3643.

STAR★METHODS

KEY RESOURCES TABLE

REAGENT or RESOURCE	SOURCE	IDENTIFIER
Biological samples		
Human adipose-derived mesenchymal stem cells	Munich Obesity BioBank (MOBB)	NA
Primary human hepatocytes	BioIVT	YNZ
Chemicals, peptides, and recombinant proteins		
MitoTracker™ Deep Red FM	Molecular Probes, Inc.	M22426
BODIPY™ 505/515	Molecular Probes, Inc.	D3921
Alexa Fluor™ 568 Phalloidin	Life Technologies Corp.	A12380
Hoechst 33342	Molecular Probes, Inc.	H3570
Wheat Germ Agglutinin, Alexa Fluor™ 555 Conjugate	Molecular Probes, Inc.	W32464
SYTO™ 14 Green Fluorescent Nucleic Acid Stain	Molecular Probes, Inc.	S7576
16% Paraformaldehyde, methanol-free	Electron Microscopy Sciences	15710-S
Hank's Balanced Salt Solution (1x), HBSS	Life Technologies Corp.	14025076
Triton X-100	Merck KGaA	X100
Phalloidin-Atto-565	Merck KGaA	94072
Critical commercial assays		
Infinium HTS assay + GSA Bead Chips	Illumina, Inc.	NA
Deposited data		
Raw data and code	GitHub	https://github.com/ClaussnitzerLab/Lipocyte-Profiler
Experimental models: Cell lines		
hWAT	Xue et al.[29]	https://doi.org/10.1038/nm.3881
hBAT	Xue et al.[29]	https://doi.org/10.1038/nm.3881
SGBS	Wabitsch et al. 2001	https://doi.org/10.1038/sj.ijo.0801520
Cas9 expressing hWAT	This paper	NA
Oligonucleotides		
guide sequences targeting: *PPARG*: ATACACAGGTGCAATCAAAG and CAACTTTGGGATCAGCTCCG; *PPARGC1A* TATTGAACGCACCTTAAGTG and AGTCCTCACTGGTGGACACG; *MFN1*: CACCAGGTCATCTCTCAAGA and TTATATGGCCAATCCCACTA; *PLIN1*: TCACGGCAGATACTTACCAG and TCTGCACGGTGTATCGAGAG; *INSR*: TTATCGGCGATATGGTGATG and AGTGAGTATGAGGATTCGGC; *IRS1* CCCAGGACCCGCATTCAAAG and CCGAAGCACTAGATCGCCGT	This paper	NA
non-targeted controls (control guide sequences): ATCAGGCCTTGTCCGTGATT; TACGTCATTAAGAGTTCAAC; GACAGTGAAATTAGCTCCCA; GATTCATACTAAACACTCTAx; CCTAGTTCATAAGCTACGCC	This paper	NA
Software and algorithms		
LipocyteProfiler	This paper	https://github.com/ClaussnitzerLab/Lipocyte-Profiler

(Continued on next page)

Continued

REAGENT or RESOURCE	SOURCE	IDENTIFIER
CRISPResso	Pinello et al.[68]	https://doi.org/10.1038/nbt.3583
PLINK	Purcell et al.[69] and Chang et al. 2015	https://doi.org/10.1086/519795 and https://doi.org/10.1186/s13742-015-0047-8
SHAPEIT2	Delaneau et al.[70]	https://doi.org/10.1038/nmeth.2307
PRS-CS	Ge et al.[71]	https://doi.org/10.1038/s41467-019-09718-5
LDpred	Vilhjálmsson et al.[72]	https://doi.org/10.1016/j.ajhg.2015.09.001
igraph	Csardi et al. 2006	https://igraph.org
Enrichr	Chen et al. 2013	https://maayanlab.cloud/Enrichr/
FastQC	Babraham Bioinformatics	https://www.bioinformatics.babraham.ac.uk/projects/fastqc/
STAR	Dobin et al.[73]	https://doi.org/10.1093/bioinformatics/bts635
DESeq2	Love et al.[74]	https://doi.org/10.1186/s13059-014-0550-8
CellProfiler 3.1.9	Carpenter et al. 2006	https://doi.org/10.1186/gb-2006-7-10-r100
Harmony 4.9	PerkinElmer Inc.	HH17000010
ARACNE	Margolin et al.[75]	https://doi.org/10.1186/1471-2105-7-S1-S7
UMAP R package 0.2.7.0	McInnes et al.[76]	https://doi.org/10.21105/joss.00861
ComplexHeatmap Bioconductor package 2.7.7	Gu et al.[77]	https://doi.org/10.1093/bioinformatics/btw313
Sample Progression Discovery (SPD)	Qui et al. 2011	https://doi.org/10.1371/journal.pcbi.1001123.g001
BEclear	Akulenko et al.[78]	https://doi.org/10.1371/journal.pone.0159921
R 3.6.1	The R Foundation for Statistical Computing	NA
Other		
CellCarrier Ultra 96 well plate, black (now: PhenoPlate™ 96-well)	PerkinElmer Inc.	#6005550
CellCarrier Ultra 96 well plate, black (now: PhenoPlate™ 96-well); collagen-coated	PerkinElmer Inc.	#6055700
Opera Phenix® High-Content Screening System	PerkinElmer Inc.	NA
Leica DMi8 microscope with HC PL APO ×63/1.40 oil objective	Leica Microsystems GmbH	NA
MGB Biobank data	Partners HealthCare hospitals	NA

RESOURCE AVAILABILITY

Lead contact
Further information and requests for resources and reagents should be directed to and will be fulfilled by the lead contact, Melina Claussnitzer (melina@broadinstitute.com).

Materials availability
This study did not generate new unique reagents.

Data and code availability
The codes are publicly available on GitHub https://github.com/ClaussnitzerLab/Lipocyte-Profiler and https://zenodo.org/record/7341916#.ZCtCjuzMKJ9. The high content imaging data are available at the Cell Painting Gallery on the Registry of Open Data on AWS (https://registry.opendata.aws/cellpainting-gallery/) under accession number cpg0011. The transcriptomics data are available on the GEO (Accession number GSE184089).

EXPERIMENTAL MODEL AND SUBJECT DETAILS

Human primary AMSC isolation/abdominal laparoscopy cohort–Munich obesity BioBank/MOBB

We obtained AMSCs from subcutaneous and visceral adipose tissue from patients undergoing a range of abdominal laparoscopic surgeries (sleeve gastrectomy, fundoplication or appendectomy). The visceral adipose tissue is derived from the proximity of the angle of His and subcutaneous adipose tissue obtained from beneath the skin at the site of surgical incision. Additionally, human liposuction material was obtained. Each participant gave written informed consent before inclusion and the study protocol was approved by the ethics committee of the Technical University of Munich (Study No 5716/13). Isolation of AMSCs was performed as previously described in.[79] For a subset of donors, purity of AMSCs was assessed as previously described in.[80] Briefly, cells were stained with 0.05μg CD34, 0.125μg CD29, 0.375μg CD31, 0.125μg CD45 per 250K cells and analyzed on CytoFlex together with negative control samples of corresponding AMSCs.

Differentiation of human AMSCs

For imaging, cells were seeded at 10K cells/well in 96-well plates (Cell Carrier, Perkin Elmer #6005550) and induced 4 days after seeding. For RNAseq, cells were seeded at 40K cells/well in 12-well dishes (Corning). Before Induction cells were cultured in proliferation medium (Basic medium consisting of DMEM-F12 1% Penicillin - Streptomycin, 33μM Biotin and 17μM Pantothenate supplemented with 0.13μM Insulin, 0.01μg/ml EGF, 0.001μg/ml FGF, 2.5%FCS). Adipogenic differentiation was induced by changing culture medium to induction medium. (Basic medium supplemented with 0.861μM Insulin, 1nM T3, 0.1μM Cortisol, 0.01 mg/ml Transferrin, 1μM Rosiglitazone, 25nM Dexamethasone, 2.5nM IBMX). On day 3 of adipogenic differentiation culture medium was changed to differentiation medium (Basic medium supplemented with 0.861μM Insulin, 1nM T3, 0.1μM Cortisol, 0.01 mg/ml Transferrin). Medium was changed every 3 days. Visceral-derived AMSCs were differentiated by further adding 2% FBS as well as 0.1mM oleic and linoleic acid to the induction and differentiation media. For isoproterenol stimulation experiments, 1uM isoproterenol was added to the differentiation media and cells treated overnight.

Primary human hepatocyte culture

Primary human hepatocytes (PHH) were purchased from BioIVT. Donor lot YNZ was used in this study. PHH were thawed and immediately resuspended in CP media (BioIVT) supplemented with torpedo antibiotic (BioIVT). Cell count and viability were assessed by trypan blue exclusion test prior to plating. Hepatocytes were plated onto collagen-coated Cellcarrier-96 Ultra Microplates (Perkin Elmer) at a density of 50,000 cells per well in CP media supplemented. Four hours after plating, media was replaced with fresh CP media. After 24 h, media was replaced with fresh CP media or CP media containing oleic acid (0.3mM) or metformin (5mM). Hepatocytes were incubated for an additional 24 h prior to processing.

MGB Biobank cohort

The MGB Biobank[81] maintains blood and DNA samples from more than 60,000 consented patients seen at Partners HealthCare hospitals, including Massachusetts General Hospital, Brigham and Women's Hospital, McLean Hospital, and Spaulding Rehabilitation Hospital, all in the USA. Patients are recruited in the context of clinical care appointments at more than 40 sites, clinics, and electronically through the patient portal at Partners HealthCare. Biobank subjects provide consent for the use of their samples and data in broad-based research. The Partners Biobank works closely with the Partners Research Patient Data Registry (RPDR), the Partners' enterprise scale data repository designed to foster investigator access to a wide variety of phenotypic data on more than 4 million Partners HealthCare patients. Approval for analysis of Biobank data was obtained by Partners IRB, study 2016P001018.

Type 2 diabetes status was defined based on "curated phenotypes" developed by the Biobank Portal team using both structured and unstructured electronic medical record (EMR) data and clinical, computational and statistical methods. Natural Language Processing (NLP) was used to extract data from narrative text. Chart reviews by disease experts helped identify features and variables associated with particular phenotypes and were also used to validate results of the algorithms. The process produced robust phenotype algorithms that were evaluated using metrics such as sensitivity, the proportion of true positives correctly identified as such, and positive predictive value (PPV), the proportion of individuals classified as cases by the algorithm.[82]

  a. Control selection criteria.
     1. Individuals determined by the "curated disease" algorithm employed above to have no history of type 2 diabetes with NPV of 99%.
     2. Individuals at least age 55.
     3. Individuals with HbA1c less than 5.7
  b. Case selection criteria.
     1. Individuals determined by the "curated disease" algorithm employed above to have type 2 diabetes with PPV of 99%
     2. Individuals at least age 30 given the higher rate of false positive diagnoses in younger individuals.

Genomic data for 30,240 participants was generated with the Illumina Multi-Ethnic Genotyping Array, which covers more than 1.7 million markers, including content from over 36,000 individuals, and is enriched for exome content with >400,000 markers missense, nonsense, indels, and synonymous variants.

METHOD DETAILS

LipocytePainting

Human primary AMSCs and PHH were plated in 96-well CellCarrier Black plates (PerkinElmer #6005550). AMSCs were differentiated for 14 days, and high content imaging was performed at day 0, day 3, day 8 and day 14 of adipogenic differentiation in replicates of 4 per donor/time point/depot (inter-replicate variance of 0.075). Primary human hepatocytes were stained after 48 h in culture, and 24h following treatment with oleic acid or metformin. On the respective day of the assay, cell culture media was removed and replaced by 0.5uM Mitotracker staining solution (1mM MitoTracker Deep Red stock (Invitrogen #M22426) diluted in culture media) to each well followed by 30 min incubation at 37°C protected from light. After 30min Mitotracker staining solution was removed and cells were washed twice with Dulbecco's Phosphate-Buffered Saline (1X), DPBS (Corning #21-030-CV) and 2.9uM BODIPY staining solution (3.8mM BODIPY 505/515 stock (Thermofisher #D3921) diluted in DPBS) was added followed by 15 min incubation at 37°C protected from light. Subsequently, cells were fixed by adding 16% Methanol-free Paraformaldehyde, PFA (Electron Microscopy Sciences #15710-S) directly to the BODIPY staining solution to a final concentration of 3.2% and incubated for 20 min at RT protected from light. PFA was removed and cells were washed once with Hank's Balanced Salt Solution (1x), HBSS (Gibco #14025076). To permeabilize cells 0.1% Triton X-100 (Sigma Aldrich #X100) was added and incubated at RT for 10 min protected from light. After Permeabilization multi-stain solution (10 units of Alexa Fluor 568 Phalloidin (ThermoFisher #A12380), 0.01 mg/ml Hoechst 33342 (In-vitrogen #H3570), 0.0015 mg/ml Wheat Germ Agglutinin, Alexa Fluor 555 Conjugate (ThermoFisher #W32464), 3uM SYTO 14 Green Fluorescent Nucleic Acid Stain (Invitrogen #S7576) diluted in HBSS) was added and cells were incubated at RT for 10 min protected from light. Finally, staining solution was removed and cells were washed three times with HBSS. Cells were imaged using a Opera Phenix High content screening system using confocal, 20× objective. Per well we imaged 25 fields.

Staining and microscopy of actin-cytoskeleton in subcutaneous AMSCs

To stain the actin cytoskeleton, and nuclei, cells were washed twice with ice-cold PBS and fixed with paraformaldehyde Roti-Histofix 4% (Roth, Karlsruhe, Germany) for 15 min. Cells were washed twice with ice-cold PBS for 5 min and incubated with ice-cold 0.1% Triton X-/PBS (Roth, Karlsruhe, Germany) for 5 min. Cells were washed twice with PBS and stained with 0.46% Bisbenzimide H 33258 (Sigma-Aldrich, Steinheim, Germany), and 1% Phalloidin-Atto-565 (Sigma-Aldrich, Steinheim, Germany). Cells were incubated for 1 h at RT in the dark. Afterward, cells were washed twice with PBS for 5 min and kept in PBS at 4°C until imaging. Images were acquired on a Leica DMi8 microscope using the HC PL APO ×63/1.40 oil objective. Images were processed using the Leica LasX software.

Isolation and adipocyte diameter determination of floating mature adipocytes

Mature adipocyte isolation was carried out as described earlier.[83] Immediately after isolation, approximately 50 μL of the adipocyte suspension was pipetted onto a glass slide and the diameter of 100 cells was manually determined under a light microscope.

CRISPR-Cas9-mediated knockout of adipocyte marker genes

We generated a hWAT cell-line stably expressing Cas9 as previously described in Shalem et al.[84] We validated the generated line by assessing Cas9 activity (90%) and adipocyte differentiation capacity using adipocyte marker gene expression and morphological profiling. CRISPR-Cas9 mediated knockdown of *PPARG*, *PPARGC1AA*, *MFN1*, *PLIN1*, *INSR*, and *IRS1* was performed in pre-adipo-cytes (5 days before differentiation) using three replicates per guide and two guides per gene (guide sequences targeting *PPARG*: ATACACAGGTGCAATCAAAG and CAACTTTGGGATCAGCTCCG; *PPARGC1A* TATTGAACGCACCTTAAGTG and AGTCCTCACTGGTGGACACG; *MFN1*: CACCAGGTCATCTCTCAAGA and TTATATGGCCAATCCCACTA; *PLIN1*: TCACGGCAGATACTTACCAG and TCTGCACGGTGTATCGAGAG; *INSR*: TTATCGGCGATATGGTGATG and AGTGAGTATGAGGATTCGGC; *IRS1* CCCAGGACCCGCATTCAAAG and CCGAAGCACTAGATCGCCGT) as well as five non-targeted controls (control guide sequences: ATCAGGCCTTGTCCGTGATT, TACGTCATTAAGAGTTCAAC, GACAGTGAAATTAGCTCCCA, GATTCATACTAAACACTCTA, CCTAGTTATAAGCTACGCC) in an 96-well arrayed format. Guide on-target efficiency was assessed using Next-generation sequencing followed by CRISPResso analysis.[68] AMSCs were stained using LipocytePainting (see above) on day 14 of differentiation. After feature extraction and QC steps (see also LipocyteProfiling), we removed samples where guide cutting efficiency was <10% or where discrepancy be-tween the two guides was equal or above 10%. For visualizations we used one non-targeted control that showed lowest standard deviation of replicates and was closest to the median of all five non-targeted controls across all LipocyteProfiler features.

QUANTIFICATION AND STATISTICAL DETAILS

LipocyteProfiling

Quantitation was performed using CellProfiler 3.1.9. Prior to processing, flat field illumination correction was performed using func-tions generated from the median intensity across each plate. Nuclei were identified using the DAPI stain and then expanded to identify

whole cells using the Phalloidin/WGA and BODIPY stains. Regions of cytoplasm were then determined by removing the Nuclei from the Cell segmentations. Speckles of BODIPY staining were enhanced to assist in detection of small and large individual Lipid objects. For each object set measurements were collected representing size, shape, intensity, granularity, texture, colocalization and distance to neighboring objects. After LipocyteProfiler (LP) feature extraction data was filtered by applying automated and manual quality control steps. First, fields with a total cell count less than 50 cells were removed. Second, every field was assessed visually and fields that were corrupted by experimental induced technical artifacts were removed. Furthermore, blocklisted features(Way, 2020), LP-features measurement category *Manders*, *RWC and Costes*, that are known to be noisy and generally unreliable were removed. Additionally, LP-features named *SmallLipidObjetcs*, that measure small objects stained by SYTO14 rather than lipid informative objects, were also removed. After filtering data were normalized per plate using a robust scaling approach[85] that subtracts the median from each variable and divides it by the interquartile range. Individual wells were aggregated for downstream analysis by cell depot and day of differentiation. Subsequent data analyses were performed in R3.6.1 and MATLAB using base packages unless noted.

To assess batch effects we visualized the data using a Principal component analysis and quantified it using a Kolmogorov-Smirnov test implemented in the "BEclear" R package.[78] Additionally we applied a k-nearest neighbor (knn) supervised machine learning based classification algorithm implemented in the "class" R package[49] to investigate the accuracy of predicting biological and technical variation. For this analysis the dataset, consisting of 3 different cell types (hWAT, hBAT, SGBS) distributed on the 96-well plate, imaged at 4 days of differentiation, was split into equally balanced testing (n = 18) and training (n = 56) sets. Accuracy of this classification model was predicted based on three different categories, i.e. cell type, batch and column of the 96-well plate. (https://github.com/ClaussnitzerLab/Lipocyte-Profiler)

For dimensionality reduction visualization Uniform manifold approximation and projection maps (UMAP) were created using the UMAP R package version 0.2.7.0[76] (https://github.com/ClaussnitzerLab/Lipocyte-Profiler). To visualize LipocyteProfiler features and their effect size ComplexHeatmap Bioconductor package version 2.7.7[77] was used (https://github.com/ClaussnitzerLab/Lipocyte-Profiler)

To identify patterns of adipocyte differentiation underlying the morphological profiles a sample progression discovery analysis (SPD) was performed using the algorithm previously described in Qiu et al.[38] Briefly, the two adipose depots were analyzed separately, and features were clustered into modules based on correlation (correlation coefficient 0.6). Minimal spanning trees (MST) were constructed for each module and MSTs of each module are correlated with each other. Modules that support common MST were selected and an overall MST based on features of all selected modules were reconstructed.

Variance component analysis was performed by fitting multivariable linear regression models - $yi \sim xi + zi + .$ - where y denotes an LipocyteProfiler feature of individual i and x, z, etc. independent variables that could confound identification of biological sources of variability of the dataset. Independent variables are experimental batch, adipose depot, passaging before freezing, season and year of AMSCs isolation, sex, age, BMI, T2D status of individual, LipocyteProfiler feature Cells_Neighbors_PercentTouching_Adjacent corresponding to density of cell seeding and identification numbers of individuals. (https://github.com/ClaussnitzerLab/Lipocyte-Profiler)

To test whether there is a difference of morphological profiles on the tail ends of polygenic risk scores (PRS) for T2D, HOMA-IR and WHRadjBMI a multi-way analysis of variance (ANOVA) was performed. Individuals belonging to top 25% and bottom 25% of PRS score distribution are categorized into a categorical variable with 2 levels, top 25% or 25% bottom, according to their PRS percentile. Differences of morphological profiles are predicted using the categorized PRS variable adjusted for sex, age, BMI and batch. Additionally linear regression models were fitted adjusted for sex, age, BMI, batch and PC1 to predict differences of morphological and cellular profiles based polygenic risk for metabolic traits. To overcome multiple testing burden p values were corrected using false positive rate (FDR) described in R package "qvalue" (qvalue, no date). Features with FDR <5% were classified to be significantly impacted by the PRS variable. (https://github.com/ClaussnitzerLab/Lipocyte-Profiler) To decrease complexity we first removed features based on effect size and measurement type/class, and second removed features that correlate r > 0.85 with at least 10% of features of remaining features (https://github.com/ClaussnitzerLab/Lipocyte-Profiler).

LipocyteProfiler feature reduction using ARACNE

Algorithm for the Reconstruction of Accurate Cellular Networks, ARACNE[26,75,86] is a software package designed to capture regulatory networks from gene expression data. The method makes use of mutual information (MI) ranking to prioritize first order relationships (also known as direct regulatory relations) among genes, and to generate accurate maps of the regulatory network. The use of MI for the prioritization of biomolecular and clinical characteristics has been demonstrated previously calculated by the algorithm can be used to prioritize interactions between other cellular and molecular characteristics.[25,27,87] In this study, we use the ARACNE algorithm to construct a graph where its nodes represent the LipocyteProfiler's features and its weighted edges represent MI between prioritized first order relations between the nodes. We then build on this network to reduce the dimensionality of the LipocyteProfiler total feature space. Since the graph is constructed based on the calculated MI, the number of significant interactions of a node can be used to: (1) identify information hubs in the graph based on the number of connectivities of the nodes. After ranking the nodes based on their number of edges, a 75% upper quantile cutoff was applied to define the information hubs, (2) identify nodes with low connectivity that share minimal information. We calculated the average of weights (MI) of outgoing edges from every node and considered this average as the MI represented by the node. By ranking the nodes based on their calculated MI and applying a 25% lower quantile cutoff, we could identify the non-hub nodes that share minimal information (Figures S1B and S1C). The characterization of these two types of nodes play an important role in reducing the dimensionality of the LipocyteProfiler feature space while mitigating the overall information loss.

We classify those LipocyteProfiler features identified as information hubs or that passed the MI cutoff as "LipocyteProfiler core features". We applied the two criteria on the total 3,005 LipocyteProfiler input features of visceral and subcutaneous derived AMSCs resulting in two sets of adipose depot-dependent LipocyteProfiler core feature sets. As a result, 986 features were labeled as LipocyteProfiler core features for visceral adipocytes and 1,002 for subcutaneous adipocytes. Between the two sets, there are 770 shared core features. The scripts for executing the ARACNE algorithm on the LipocyteProfiler features and the post processing steps for identifying the LipocyteProfiler core features are available through the GitHub page (https://github.com/ClaussnitzerLab/Lipocyte-Profiler).

Generating of average cells
For each group of interest, cells were pooled and divided into 100 clusters via K-Means clustering (scikit-learn). Individual cells were then sampled from the cluster closest to a theoretical point representing the mean of all object measurements, as determined by a Euclidean distance matrix.

RNA-seq
RNA-seq data were processed using FastQC[88] and spliced reads were aligned to human genome assembly (hg19) using STAR[73] followed by counting gene levels using Rsubread R package.[89] Next, raw read counts were normalized using the DESseq2 R package.[74] For differential expression analysis on the tail ends of polygenic risk scores (PRS) for HOMA-IR a multi-way analysis of variance (ANOVA) was performed on subset of 512 genes (GSEA hallmark gene sets for adipogenesis, fatty acid metabolism and glycolysis). Individuals belonging to top 25% and bottom 25% of PRS score distribution are categorized into a categorical variable with 2 levels, top 25% or 25% bottom, according to their PRS percentile. Differences in transcriptional profiles are predicted using categorized PRS variable adjusted for sex, age, BMI and batch. To overcome multiple testing burden p values were corrected using false positive rate (FDR) described in R package "qvalue" (qvalue). Genes with FDR <10% were classified to be significantly impacted by PRS and were uploaded to Enrichr to analyze them as a gene list against the WikiPathways. (https://github.com/ClaussnitzerLab/Lipocyte-Profiler)

Gene expression and LipocyteProfiler feature network
A linear regression model was fitted of 2,760 LP-features and global transcriptome RNA-seq data adjusted for sex, age, BMI and batch in subcutaneous AMSCs at day 14 of differentiation. Gene LP features associations were declared to be significant when passing the FDR cut-off of FDR< 0.01% (FDR<0.1%). LP features belonging to Cells category were used for further analysis. Associations between genes and LP features were visualized using "igraph" R package (Csardi, Nepusz and Others, 2006 - https://igraph.org/) (https://github.com/ClaussnitzerLab/Lipocyte-Profiler). Genes that are connected to top scoring LP features were uploaded to Enrichr to analyze them as a gene list against WikiPathways or BioPlanet. Adipocyte marker genes, *SCD*, *PLIN2*, *LIPE*, *INSR*, *GLUT4 and TIMM22*, were chosen to demonstrate morphological profiles matching their known pathways, by identifying LP features that associate with those genes with a global significant level of FDR<5%. (https://github.com/ClaussnitzerLab/Lipocyte-Profiler)

Quality control of genotyping data
Genotyping of all samples was performed in two separate batches using the Infinium HTS assay on Global Screening Array beadchips. Since the two sets of samples were genotyped with different versions of the beadchips and in different batches, we Qced, imputed, and generated the genome-wide polygenic scores separately and combined the results afterward.

A 3-step quality control protocol was applied using PLINK,[69,90] and included 2 stages of SNP removal and an intermediate stage of sample exclusion. The exclusion criteria for genetic markers consisted of: proportion of missingness ≥ 0.05, HWE p $\leq 1 \times 10{-20}$ for all the cohort, and MAF <0.001. This protocol for genetic markers was performed twice, before and after sample exclusion. For the individuals, we considered the following exclusion criteria: gender discordance, subject relatedness (pairs with PI-HAT ≥ 0.125 from which we removed the individual with the highest proportion of missingness), sample call rates ≥ 0.02 and population structure showing more than 4 standard deviations within the distribution of the study population according to the first seven principal components. After QC, 35 subjects remained for the analysis for which we had matched LipocyteProfiler imaging data.

Genotypes were phased with SHAPEIT2,[70] and then performed genotype imputation with the Michigan Imputation server, using Haplotype Reference Consortium (HRC)[91] as reference panel. We excluded variants with an info imputation r-squared <0.5 and a MAF <0.005.

Constructing PRSs
Genome-wide polygenic scores were computed using PRS-CS[71] and using the "auto" parameter to specify the phi shrinkage parameter. We computed the PRS-CS polygenic scores for the following traits: T2D,[51] BMI, waist-to-hip ratio adjusted and unadjusted by BMI, and stratified by sex and combined.[54] Genome-wide PRS for HOMA-IR were computed with LdPred[72] using summary statistics from Dupuis et al. (Dupuis et al., 2010). Process-specific PRSs were constructed based on five clusters defined in Udler et al.[59] by selecting the SNPs that had weight larger than 0.75 for each of a given cluster.

All PRSs were tested for association with T2D and with BMI using the 30,240 MGB Biobank samples from European Ancestry defined based on self-reported and principal components.